Exp.-Nr. **A2-07/16**
Eingang:
an PAC: 31.08.2016

Mainz Microtron MAMI

A2 Collaboration at MAMI
Spokespersons: P. Pedroni, A. Thomas

Proposal for an Experiment

"Photoproduction of the $\Lambda(1405)$ Hyperon"

Spokespersons for the Experiment :
D. Werthmüller (University of Glasgow, Glasgow, United Kingdom)
R.A. Schumacher (Carnegie Mellon University, Pittsburgh, USA)

Abstract of Physics :
We propose to use the high current photon beam available at A2 to produce the isosinglet $\Lambda(1405)1/2^-$ hyperon at threshold via $\gamma p \to K^+\Lambda(1405)$. Its nature is still controversial and actively debated. Since the only available photoproduction data from CLAS are lacking in precision in the $\Sigma^0\pi^0$ decay channel, we propose a new independent measurement of this most important pure $I = 0$ final state including the unmeasured beam-helicity observable $I^\odot$. In addition, the excellent photon detection acceptance of the A2 setup will offer the opportunity for a first measurement of the radiative decays of the $\Lambda(1405)$, which will provide clean and stringent constraints for model descriptions in terms of, e.g., unitary chiral perturbation theory.

Abstract of Equipment :
The experiment requires a tagged photon beam above the $\Lambda(1405)$ production threshold using the end-point tagger (EPT). The charged kaons will be detected using the in-crystal decay technique in the calorimeters. Separation of charged pions and protons using the particle identification detector (PID) and the TAPS vetos/Pizza detector will be important for the complex and high multiplicity final states. The installation of additional detectors (Čerenkov) to improve the kaon detection efficiency will be investigated.

MAMI Specifications :

beam energy	1604 MeV
beam polarization	polarized

Photon Beam Specifications :

tagged energy range	above 1450 MeV (EPT)
photon beam polarization	circularly polarized

Equipment Specifications :

detectors	EPT, CB, TAPS, PID, Pizza detector
target	liquid hydrogen

Beam Time Request :

set-up/test with beam	150 hours
data taking	1000 hours

List of participating authors:

- **Institut für Physik, University of Basel, Switzerland**
  S. Abt, S. Garni, M. Günther, A. Käser, B. Krusche, S. Lutterer, M. Oberle, Th. Strub, N.K. Walford, L. Witthauer
- **Institut für Experimentalphysik, University of Bochum, Germany**
  G. Reicherz
- **Helmholtz–Institut für Strahlen- und Kernphysik, University of Bonn, Germany**
  F. Afzal, R. Beck, K. Spieker, A. Thiel
- **JINR, Dubna, Russia**
  N.S. Borisov, A. Lazarev, A. Neganov, Yu.A. Usov
- **SUPA School of Physics, University of Edinburgh, UK**
  M. Bashkanov, S. Kay, D.P. Watts, L. Zana
- **SUPA School of Physics and Astronomy, University of Glasgow, UK**
  J.R.M. Annand, D. Hamilton, D.I. Glazier, S. Gardner, K. Livingston, R.Macrae , I.J.D. MacGregor, C. Mullen, D. Werthmüller
- **Department of Astronomy and Physics, Saint Mary's University Halifax, Canada**
  A.J. Sarty
- **Racah Institute of Physics, Hebrew University of Jerusalem, Israel**
  G. Ron
- **Kent State University, Kent, USA**
  C.S. Akondi, D.M. Manley
- **Institut für Kernphysik, University of Mainz, Germany**
  P. Achenbach, H.J. Arends, M. Biroth, F. Cividini, A. Denig, P. Drexler, M.I. Ferretti-Bondy, W. Gradl, V.L Kashevarov, P.P. Martel, A. Neiser, E. Mornacchi, M. Ostrick, S.N. Prakhov, V. Sokhoyan, C. Sfienti, O. Steffen, M. Thiel, A. Thomas, S. Wagner, J. Wettig, M. Wolfes
- **University of Massachusetts, Amherst, USA**
  R.Miskimen, A. Rajabi
- **Institute for Nuclear Research, Moscow, Russia**
  G. Gurevic, R. Kondratiev, V. Lisin, A. Polonski
- **INFN Sezione di Pavia, Pavia, Italy**
  A. Braghieri, S. Costanza, P. Pedroni
- **Department of Physics, Carnegie Mellon University, Pittsburgh, USA**
  R.A. Schumacher
- **Department of Physics, University of Regina, Canada**
  Z. Ahmed, G.M. Huber, D. Paudyal
- **Mount Allison University, Sackville, Canada**
  D. Hornidge
- **Tomsk Polytechnic University, Tomsk, Russia**
  A. Fix

- **George Washington University, Washington, USA**
  W.J. Briscoe, C. Collicott, E.J. Downie, I.I. Strakovski
- **Rudjer Boskovic Institute, Zagreb, Croatia**
  M. Korolija, I. Supek

1 Motivation

1.1 Introduction

The $\Lambda(1405)1/2^-$ is a $S = -1$, $I = 0$ hyperon resonance that lies just below the $\bar{K}N$ threshold ($E^{thr}_{K^-p} \approx 1432$ MeV) and decays via strong interaction to $(\Sigma\pi)^0$ pairs. The $\bar{K}N$ and the $\Sigma\pi$ channels are coupled via unitarity and it was first shown in 1959 by Dalitz and Tuan [1] that the characteristics of the K^-p scattering amplitude lead to a resonance in the $\Sigma\pi$ channel. Soon after this study an excess of events in the $(\Sigma\pi)^0$ system was observed in bubble chamber experiments measuring $K^-p \to \Sigma^+\pi^-\pi^-\pi^+$ and $K^-p \to \Sigma^-\pi^+\pi^+\pi^-$ [2]. No excess was found in the $(\Sigma\pi)^{\pm\pm}$ systems and an isospin of $I = 0$ was deduced from the count ratio of the three different $(\Sigma\pi)^0$ observations using the following isospin representations:

$$|\Sigma^+\pi^-\rangle = \sqrt{\frac{1}{3}}\,|0,0\rangle + \sqrt{\frac{1}{2}}\,|1,0\rangle + \sqrt{\frac{1}{6}}\,|2,0\rangle \tag{1}$$

$$|\Sigma^-\pi^+\rangle = \sqrt{\frac{1}{3}}\,|0,0\rangle - \sqrt{\frac{1}{2}}\,|1,0\rangle + \sqrt{\frac{1}{6}}\,|2,0\rangle \tag{2}$$

$$|\Sigma^0\pi^0\rangle = -\sqrt{\frac{1}{3}}\,|0,0\rangle + \sqrt{\frac{2}{3}}\,|2,0\rangle \tag{3}$$

It should be noted that, neglecting $I = 2$ contributions, the $\Sigma^0\pi^0$ system is a pure $I = 0$ state whereas the charged $\Sigma\pi$ systems have $I = 1$ contributions as well. This leads for example to the complication of the $\Sigma(1385)$ $I = 1$ resonance contributing to the charged $\Sigma\pi$ channels. Therefore, the $\Sigma^0\pi^0$ channel provides the cleanest way to study the $\Lambda(1405)$.

Today the $\Lambda(1405)$ is listed as a 4-star state in the baryons listing of the PDG [3] but despite having the maximum rating, the exact nature of this state is still not resolved. This is mainly caused by two puzzles.

First, most simple three-quark models [4, 5] fail to describe the low mass of this state when compared to the situation in the nucleon sector (see Fig. 1). The p-wave excitation of the nucleon ground state $N(1535)1/2^-$ generates a mass difference of about 600 MeV whereas the corresponding difference in the Λ sector is less than half of this. In addition, there is a considerable mass gap between the spin-orbit partners $\Lambda(1405)1/2^-$ and $\Lambda(1520)3/2^-$ in contrast to the near-degeneracy of the corresponding nucleon resonances $N(1535)1/2^-$ and $N(1520)3/2^-$. These issues, however, can be coped with by more sophisticated quark models, e.g., a quark-diquark approach in a relativistic quark model inspired by the heavy quark sector, in which the $\Lambda(1405)$ can be naturally reproduced [6]. Alternative descriptions include also exotic configurations such as compact pentaquarks [7] and hybrids [8].

The second enigma about the $\Lambda(1405)$ is the claimed two-pole structure [9–12]. This is illustrated in Fig. 2 by the example of the elastic $\bar{K}N$ scattering amplitude. The two poles in the complex energy plane both contribute to the amplitude and form a single bump on the real axis. Therefore, measured observables will always have contributions from two poles. The lower wider state around 1325 MeV seems to couple more strongly to $\pi\Sigma$, while the higher lying one located around 1430 MeV close to the $\bar{K}N$ threshold is more narrow and has a stronger coupling to $\bar{K}N$. There are counterarguments to the two-pole scenario [13] but it can be shown [14] that very recent results of lattice QCD calculations [15] seem to support this picture.

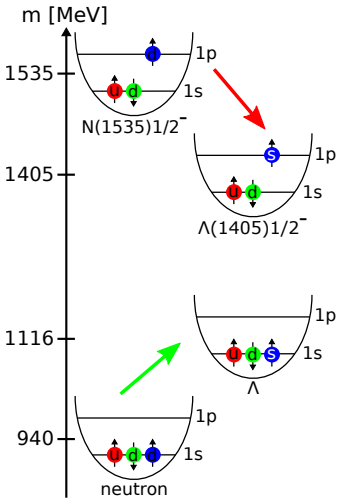

Figure 1: Comparison of the ground state and the first p-wave excited state in the simple quark model of the nucleon and the Λ sector. Despite the s-quark, the $\Lambda(1405)$ is lighter than its $N(1535)$ counterpart.

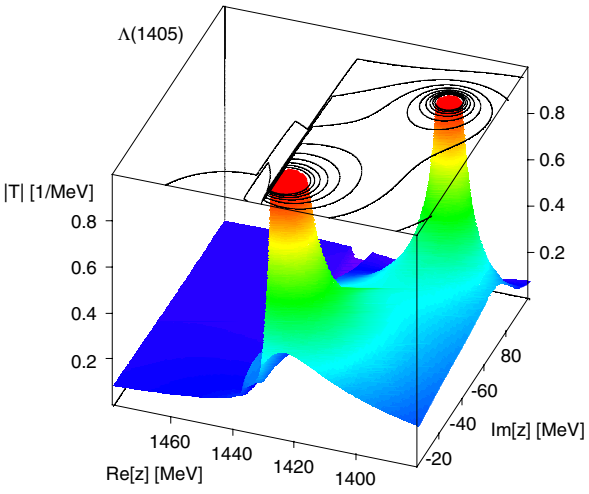

Figure 2: Two-pole structure of the $\Lambda(1405)$ resonance in the absolute value $|T|$ of the elastic $\bar{K}N$ scattering amplitude. The two poles produce one single broad bump on the real axis. Taken from [12].

Besides experiments with meson beams and bubble chambers [16, 17] the $\Lambda(1405)$ was also studied in photoproduction already in the 1970s [18] via the t-channel dominated reaction

$$\gamma p \to K^+ \Lambda(1405) \tag{4}$$

As an example, the $\Lambda(1405)$ production via the K^--exchange contribution is shown in Fig. 3. Theoretical attention to $\Lambda(1405)$-photoproduction starting in the late 1990s [19, 20] was followed only recently by measurements at LEPS [21, 22] and especially at the CLAS experiment [23–25], which denoted a huge step forward in gaining more experimental data about the $\Lambda(1405)$. For example, spin and parity were measured directly for the first time [25] and positions and widths of both resonance poles could be extracted [26–28] using chiral unitary theory, which emerged as the common framework to describe dynamics related to the $\Lambda(1405)$ (see [12] for a review).

As mentioned before, theoretical activities concerning the $\Lambda(1405)$ are numerous, coming from fields such as chiral unitary perturbation theory and lattice QCD. In a very recent work [29], also Regge theory was used to analyze the latest estimates of the pole positions suggesting that the higher-lying pole is consistent with a conventional three-quark

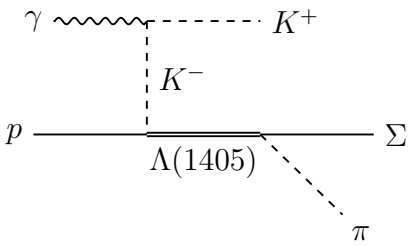

Figure 3: K^--exchange contribution to $\gamma p \to K^+ \Lambda(1405)$ in the t-channel, where the $\Lambda(1405)$ is formed via scattering of the off-shell K^- on the proton.

picture while the nature of the lower-lying pole seems to be nonordinary. This continuing interest from the theory community motivates thus more experimental attention to perform further and more precise measurements.

Despite the fact of the CLAS data being of unprecedented quality, new measurements could improve on the following points. First, the data for the most important final state $\pi^0\Sigma^0$ concerning the study of the $\Lambda(1405)$ were obtained without detection of the three decay photons, leading to a decrease in statistics due to rigorous cuts in the event selection. In addition, despite having applied stringent cuts, sufficient background rejection could not be guaranteed [23]. Second, as delicate experimental parameters, such as detector acceptance and photon flux, enter directly into the normalized $m(\Sigma\pi)$ distributions, it is necessary to conduct a second measurement at a different experiment to eliminate effects from those sources of systematic uncertainties. Finally, a high statistics measurement very close to threshold would be desirable as it simplifies the interpretation due to the less complex situation in this energy region. For example, background contributions from higher mass hyperon and kaon resonances are not present at threshold.

Therefore we propose a new experiment to be performed at A2 that will provide a significant and independent contribution to the experimental database. It will focus on areas where the A2 experiment has advantages compared to other experiments. Namely, we propose to produce the $\Lambda(1405)$ in photoproduction via $\gamma p \to K^+\Lambda(1405)$ and to measure the following observables:

1. $m(\Sigma^0\pi^0)$ and $m(\Sigma^+\pi^-)$ invariant mass distributions ('line shapes')
2. The beam-helicity asymmetry $I^\odot$ of $\vec{\gamma}p \to K^+\Sigma^0\pi^0$ and $\vec{\gamma}p \to K^+\Sigma^+\pi^-$ with circularly polarized photons
3. Signal search and potential determination of $\Gamma_{Y\gamma}/\Gamma_{\Sigma^0\pi^0}$ for the $\Lambda(1405) \to Y\gamma$ radiative decays with $Y = \{\Lambda, \Sigma^0\}$

The next sections will present those physics goals in more detail discussing previous measurements, the current status of both experimental and theoretical research and future contributions from other experiments.

1.2 $\Sigma^0\pi^0$ and $\Sigma^+\pi^-$ line shapes

Due to the two poles contributing to the $\Lambda(1405)$ resonance, the distribution of the $m(\Sigma\pi)$ invariant mass ('line shape') depends on the reaction the $\Lambda(1405)$ is produced in, giving more weight to either the lower or higher lying resonance pole. In addition, according to Eqs. 1–3, the different $(\Sigma\pi)^0$ isospin states are sensitive to the isospin structure of the production amplitude.

The $\Sigma^0\pi^0$ channel bears the advantage that only isospin $I = 0$ amplitudes contribute (apart from negligible non-resonant $I = 2$ terms, see Eq. 3), which facilitates the theoretical interpretation of experimental data, while the nearby $\Sigma^0(1385)$ resonance decaying into $\Sigma^+\pi^-$ and $\Sigma^-\pi^+$ makes an isolated study of the $\Lambda(1405)$ in those decay channels more difficult. Unfortunately, most older experiments were not able to measure the neutral pion and the decay photon from the $\Sigma^0 \to \Lambda\gamma$ decay in the $\Sigma^0\pi^0$ final state. For example, older bubble chambers experiments using π^- [16] and K^- beams [17] were only able to extract the line shapes of the $\Sigma^\pm\pi^\mp$ final states.

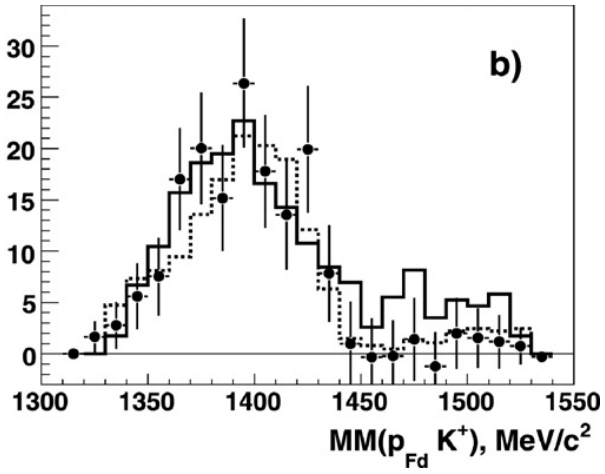

Figure 4: ANKE $pp \to pK^+\Sigma^0\pi^0$ results (points) compared to $\pi^- p \to K^0(\Sigma\pi)^0$ [16] (solid line) and $K^- p \to \pi^+\pi^-\Sigma^+\pi^-$ [17] (dotted line).

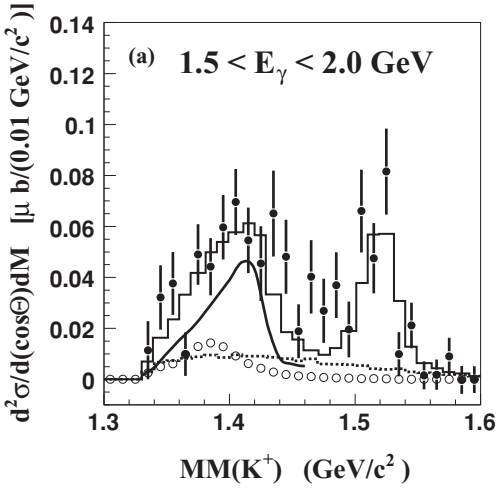

Figure 5: LEPS K^+ missing mass of $\gamma p \to K^+\Lambda(1405)$, $\Lambda(1405) \to \Sigma^\pm\pi^\mp$ event candidates [22]. The theoretical line shape from [19] was fitted along with other contributions to the data.

The Crystal Ball collaboration was able to show the presence of the $\Lambda(1405)$ in the $\Sigma^0\pi^0$ system in the measurement of $K^- p \to \pi^0\pi^0\Sigma^0$ [30]. However, due to the two indistinguishable π^0-meson this reaction is less suited to study the $\Lambda(1405)$ in the $\Sigma^0\pi^0$ distribution.

More recently, the $(\Sigma\pi)^0$ line shapes were also studied in *pp* collisions at the ANKE [31] and HADES [32] experiments. While the result of the $\Sigma^0\pi^0$ channel obtained at ANKE were found to be in reasonable agreement with the older meson-beam bubble chamber data (see Fig. 4), the $\Sigma^\pm\pi^\mp$ distributions measured by HADES differ from those older results. This illustrates the influence of the different production mechanisms and final states.

The line shapes in the $\Sigma^\pm\pi^\mp$ channels were also studied in photoproduction experiments at LEPS [21, 22]. The result of the lower photon energy bin shown in Fig. 5 shows good agreement with the theoretical calculation by Nacher *et al.* [19]. Finally, the CLAS collaboration obtained high statistics data from photoproduction measuring all three $(\Sigma\pi)^0$ isospin channels [23]. The line shapes closest to threshold and the kinematic region accessible with the proposed A2 experiment are shown in Fig. 6. As mentioned before, the $\Sigma^0\pi^0$ invariant mass distribution suffers from higher systematic and statistical uncertainties compared to the $\Sigma^\pm\pi^\mp$ channels. This is caused by the very limited to nonexistent photon detection efficiency of the CLAS detector, which was optimized for the detection of charged particles. In this respect the A2 experiment provides a completely complementary experimental setup being optimized for photon detection in almost the complete solid angle with still acceptable capabilities for the detection of charged particles.

The CLAS photoproduction data were found to be valuable input for unitary chiral approaches in terms of extracting the two $\Lambda(1405)$ pole positions [26, 27] and eliminating solutions that describe the existing hadronic data equally well [28]. Therefore, new data of the proposed experiment could be easily analyzed by those groups using existing frameworks.

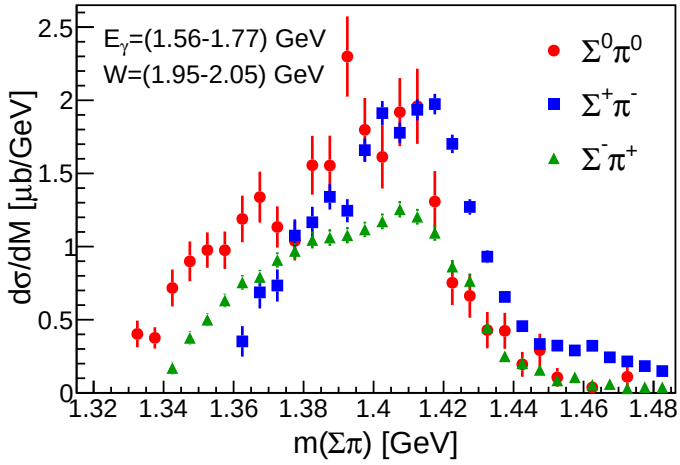

Figure 6: $(\Sigma\pi)^0$ line shapes measured by the CLAS collaboration [23] via $\gamma p \to K^+(\Sigma\pi)^0$ in the photon energy bin closest to threshold. The error bars represent only the statistical uncertainties.

1.3 Beam-helicity asymmetry $I^\odot$ of $\vec{\gamma}p \to K^+(\Sigma\pi)^0$

The beam-helicity asymmetry $I^\odot$ is a polarization observable in photoproduction defined for three-body final states, e.g. $N\pi\pi$ [33], that can be measured with a circularly polarized beam and an unpolarized target. It is defined as

$$I^\odot(\Phi) = \frac{d\sigma^+ - d\sigma^-}{d\sigma^+ + d\sigma^-} = \frac{1}{P_\gamma}\frac{N^+ - N^-}{N^+ + N^-}, \tag{5}$$

with the differential cross sections $d\sigma^\pm$ for the two photon helicity states, the degree of circular polarization of the photon P_γ and an angle Φ that can be defined in various ways in the center-of-mass system of the photon and the initial state nucleon. For $\gamma p \to p\pi\pi$ sensitivity to small contributions via interference terms was found [34]. In addition, the experimental access to this observable is particularly straightforward since all normalization factors cancel in the ratio, apart from detection efficiencies when integrated over angles or photon beam energies. Therefore, the experimental extraction only relies on the observed counts $N^\pm(\Phi)$ for the two beam helicity states.

In double-pion photoproduction $I^\odot$ has been measured with the A2 experiment for several reactions [35–37]. The degree of longitudinal polarization of the electrons at MAMI is usually $P_{e^-} \approx 70$–85% and is transferred to the circular polarization of the photons according to Olsen and Maximon [38]. In the energy range covered by the endpoint tagger for the proposed experiment, this basically translates into a constant values for P_γ that is very close to P_{e^-}.

There are no measurements known to the authors of the observable $I^\odot$ for the reactions $\vec{\gamma}p \to K^+(\Sigma\pi)^0$. On the theory side, calculations exists for $\gamma N \to K\bar{K}N$, where sensitivity of certain observables to the $\Lambda(1405)$ coupling to $\bar{K}N$ was found and measurements of $K\Sigma\pi$ final states were encouraged [39].

1.4 $\Lambda(1405)$ radiative decays

A clean way of probing the structure of baryons is the study of their radiative decays by emission of a photon. The decay scheme for the low-lying hyperon states is shown in

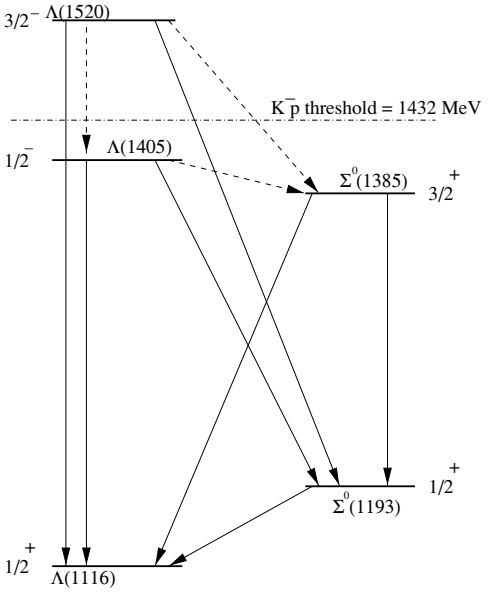

Figure 7: Radiative decay scheme of low-lying hyperon states. Suppressed transitions are denoted by the dashed lines. Taken from [40].

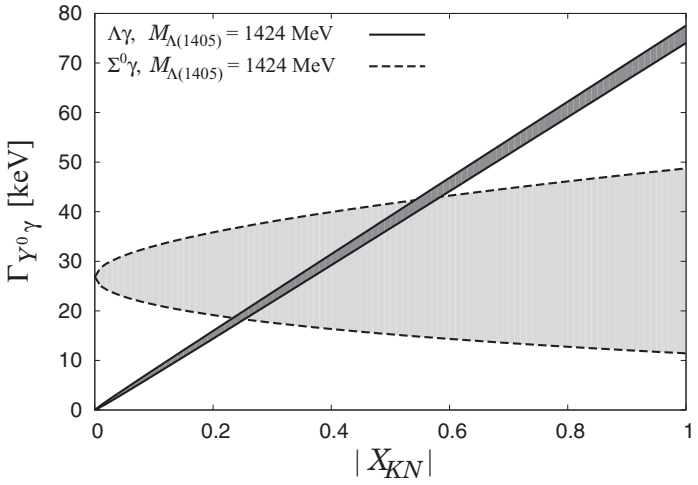

Figure 8: Radiative decay widths of the $\Lambda(1405)$ as functions of the absolute value of the $\bar{K}N$ compositeness for $m_{\Lambda(1405)} = 1424$ MeV [41].

Fig. 7. For the $\Lambda(1405)$ an early calculation [42] within the nonrelativistic quark model [4] obtained

$$\Gamma_{\Lambda\gamma} = 143 \text{ keV} \qquad \Gamma_{\Lambda\gamma}/\Gamma = 2.83 \times 10^{-3}$$
$$\Gamma_{\Sigma^0\gamma} = 91 \text{ keV} \qquad \Gamma_{\Sigma^0\gamma}/\Gamma = 1.80 \times 10^{-3}$$

with $\Gamma = (50.5 \pm 2.0)$ MeV [3]. These values are very small and pose a challenge to experiments — yet today there are still no experimental data available that were directly measured. There is a model-dependent determination [43] of the radiative widths extracted from measurements of the decays of kaonic hydrogen [44] which found even smaller values:

$$\Gamma_{\Lambda\gamma} = (27 \pm 8) \text{ keV} \qquad \Gamma_{\Lambda\gamma}/\Gamma = (5.35 \pm 1.60) \times 10^{-4}$$
$$\Gamma_{\Sigma^0\gamma,1} = (10 \pm 4) \text{ keV} \qquad \Gamma_{\Sigma^0\gamma,1}/\Gamma = (1.98 \pm 0.80) \times 10^{-4} \text{ or}$$
$$\Gamma_{\Sigma^0\gamma,2} = (23 \pm 7) \text{ keV} \qquad \Gamma_{\Sigma^0\gamma,2}/\Gamma = (4.55 \pm 1.40) \times 10^{-4}.$$

Several models describing the $\Lambda(1405)$ predict very different values for the two decay widths and in particular for their ratio. Namely, by using the two-pole results from chiral unitary theories, it was found that the ratio $\Gamma_{\Lambda\gamma}/\Gamma_{\Sigma^0\gamma}$ is reversed for the lower and the higher-lying pole [45]. Hence, experimental data on the radiative decay widths provide an excellent test of the conjectured two-pole structure or even speculative five-quark components [46]. In another work [41], a relation between the compositeness, which is a measure for the amount of the $\bar{K}N$ component inside the $\Lambda(1405)$, and the radiative decay width is established. The relation for both radiative decays is shown in Fig. 8 evaluated for a $\Lambda(1405)$ mass of 1424 MeV. This value corresponds to the higher-lying pole, where the relation is more striking. Due to cancelling $\Sigma^{\pm}\pi^{\mp}$ terms in the $\Lambda\gamma$ decay mode, the K^-p component dominates this decay resulting in a linear relationship between $\Gamma_{\Lambda\gamma}$ and

the $\bar{K}N$ compositeness. Using this calculation and a direct measurement of $\Gamma_{\Lambda\gamma}$ from photoproduction, the meson-baryon component in the $\Lambda(1405)$ could thus be estimated.

The authors of [41] also conduct a reevaluation of the $\Lambda(1405)$ radiative width in the chiral unitary approach with updated parameters and obtain the following values:

$$\Gamma_{\Lambda\gamma} = 31 \text{ keV (lower pole)} \qquad \Gamma_{\Lambda\gamma} = 96 \text{ keV (higher pole)} \tag{6}$$

$$\Gamma_{\Sigma^0\gamma} = 94 \text{ keV (lower pole)} \qquad \Gamma_{\Sigma^0\gamma} = 60 \text{ keV (higher pole)} \tag{7}$$

In view of all those possibilities on the theoretical side, experimental input from a direct measurement of the radiative decay widths is urgently needed. More recent attempts to measure the radiative decays of the $\Lambda(1405)$ in the CLAS experiment [40, 47] failed due to contamination from the overlapping $\Sigma^0(1385)$ resonance and the lack of detecting the radiated photon. Here again, the A2 setup with its excellent photon detection capabilities and high solid angle coverage could provide a great opportunity for a new attempt to observe and quantity the radiative decays of the $\Lambda(1405)$.

1.5 Competing experiments

There is an ongoing interest to study the $\Lambda(1405)$ at several experiments worldwide. Information about the low energy K^-p interaction was obtained in the SIDDHARTA experiment at DAΦNE [48] by studying kaonic hydrogen. An upgrade to this experiment measuring the K^-d interaction seems to be planned [28]. The AMADEUS experiment, which was part of the KLOE detector located at the same facility, published prelimary results of the $\Sigma^0\pi^0$ line shape [49].

At J-PARC there are continuing activities related to strangeness physics and the $\Lambda(1405)$ at various experiments (E31/E42/E45) using π^- and K^- beams. For example, the E31 collaboration is working on $(\Sigma\pi)^0$ line shape results [50] and the E45 collaboration with the HypTPC detector is planning measurements of the $\Lambda(1405)$ radiative decay [51]. As the setup seems to be incapable of photon detection, the experiment will rely on good momentum resolution of the charged particles to use the missing energy technique for an indirect measurement of the radiative decay.

Competing photoproduction experiments using beam energies up to $\sim$3 GeV will be LEPS2 at SPring-8 [52], especially once the new spectrometer based on the BNL-E949 solenoid will be operational, and the BGO-OD experiment at ELSA [53]. The latter was specifically built for the study of hyperon resonances with excellent kaon detection capabilities in forward direction although the detection is restricted to quite a small solid angle. Also, photons cannot be detected in this region and the available photon beam intensity is lower compared to MAMI. In addition, simulations (see Sec. 2.2) have shown that a considerable amount of kaons and protons coming from the reactions of interest are going to regions where they cannot be detected or not very precisely measured in this experiment.

Finally, photoproduction experiments with beam energies above 3 GeV will be the next generation experiments GlueX and CLAS12 at the Thomas Jefferson National Accelerator Facility (TJNAF). At CLAS12, quasi-real tagged photons will be available via the forward tagger with energies normally around 6.5–10.5 GeV. The very high momentum kaons in forward direction originating from the t-channel production mechanism may be detected in CLAS12 but the decay photons going beyond 35 degrees in lab polar angle will not

be detected [54]. This will result in a low detection efficiency and higher background contamination. The hermetic GlueX detector has good photon detection capabilities over a large part of the solid angle but the discrimination of high energetic kaons will only be available in 2018 [55].

2 Proposed experiment

The proposed experiment aims at measuring $\vec{\gamma}p \to K^+\Lambda(1405)$ with a circularly polarized photon beam and an unpolarized liquid hydrogen (LH_2) target to achieve the physics goals presented in Secs. 1.2–1.4. This will lead to the following primary final states:

(R1)	$\Lambda(1405) \to \Sigma^0\pi^0$	$\Sigma^0 \to \Lambda\gamma$	$\Lambda \to p\pi^-$	$\to K^+p\pi^-3\gamma$
(R2)	$\Lambda(1405) \to \Sigma^+\pi^-$	$\Sigma^+ \to p\pi^0$		$\to K^+p\pi^-2\gamma$
(R3)	$\Lambda(1405) \to \Lambda\gamma$		$\Lambda \to p\pi^-$	$\to K^+p\pi^-\gamma$
(R4)	$\Lambda(1405) \to \Sigma^0\gamma$	$\Sigma^0 \to \Lambda\gamma$	$\Lambda \to p\pi^-$	$\to K^+p\pi^-2\gamma$

It can be seen that two final states are identical and the others only differ in the number of photons. Therefore, fully exclusive measurements are inevitable to discriminate the different event candidates and a high angular coverage for photons, as provided by the A2 setup, is essential to minimize event contamination caused by undetected particles, especially photons.

The A2 setup offers the possibility to exploit the $\Lambda \to n\pi^0$ decay in addition to $\Lambda \to p\pi^-$ as done before using the Crystal Ball detector [30]. This will lead to alternative event samples for reactions (R1)–(R4), albeit with lower statistics due to the smaller branching ratio of the neutral Λ decay, the lower detection efficiency for neutrons and the higher cluster multiplicity. Nevertheless, these additional events could be useful for cross checks.

On the other hand, it will most certainly not be possible to measure the second charged $\Lambda(1405) \to \Sigma^-\pi^+$ decay since the $\Sigma^- \to n\pi^-$ leads to the two most problematic particles for the A2 setup. The energy of neutrons cannot be measured and the reconstructed energies of π^--mesons have large uncertainties. One of those particles in the final state can be handled by calculating its energy from kinematics and the energies of the other particles. This will not be possible if there are two of them.

Tab. 1 gives an overview of the decays and the corresponding branching ratios of all involved hyperons.

2.1 Experimental setup and particle detection

The experiment will be performed using available A2 equipment. Due to the high $\Lambda(1405)$ production threshold of $E_\gamma \approx 1450$ MeV the electron beam delivered by MAMI should have the maximum energy of 1604 MeV. In this configuration, the standard Glasgow photon tagger [56] can only tag photons up to ∼1490 MeV. This leads to a tagged range in the region of interest of only 40 MeV, where the production cross section is still very small. The so-called endpoint tagger (EPT) [57] was specifically constructed to cover the very high photon energy region of the A2 bremsstrahlung spectrum. It can be configured to cover photon energies from 1450–1590 MeV with a resolution of 2.7–3 MeV [58]. Parallel

	$\Lambda(1405)$	$\Sigma^0(1385)$	Λ	Σ^0	Σ^+	Σ^-
$\Sigma^+\pi^-$	33%[1]	5.9%[1]	—	—	—	—
$\Sigma^-\pi^+$	33%[1]	5.9%[1]	—	—	—	—
$\Sigma^0\pi^0$	33%[1]	—	—	—	—	—
$\Lambda\pi^0$	—	87%	—	—	—	—
$\Lambda\gamma$	?	1.25%	—	100%	—	—
$\Sigma^0\gamma$	?	?	—	—	—	—
$p\pi^-$	—	—	64%	—	—	—
$n\pi^0$	—	—	36%	—	—	—
$p\pi^0$	—	—	—	—	52%	—
$n\pi^+$	—	—	—	—	48%	—
$n\pi^-$	—	—	—	—	—	100%

Table 1: Decay branching ratios Γ_i/Γ of the involved hyperons. [1]assuming isospin symmetry. All values from [3].

running along with the main tagger is not possible, therefore experiments running with the EPT require a modification of the A2 beamline. During 2014, a series of experiments dedicated to the study of η'-decays have taken place [59], in which the EPT was used. Parts of the data obtained in these measurements have been analyzed for the preparation of this proposal and were found to be very useful for the determination of the running conditions for the proposed experiment (see Sec. 2.5).

The main detector setup is shown schematically in Fig. 9. The bremsstrahlung photons will impinge on the liquid hydrogen target installed in the center of the Crystal Ball (CB) detector [60]. It consists of two hemispheres with in total 672 optically insulated NaI(Tl) crystals of 15.7 radiation length thickness, covering all azimuthal angles for the polar angle range $20° < \theta < 160°$. All crystals point towards the center of the sphere. The distance from the center to the detector modules is 25 cm. The energy resolution for photons can be described as $\Delta E/E = 2\%/(E[\text{GeV}])^{0.36}$ while typical angular resolutions are $\Delta\theta = 2°$–$3°$ and $\Delta\phi = 2°$–$4°$ [61]. The multi-wire proportional chamber (MWPC) surrounding the PID provides basic tracking and can be used improve the angular resolution of charged particles in CB.

The forward hole of CB is covered by the hexagonal TAPS wall, which is made of 366 hexagonally shaped BaF_2 crystals with a thickness of 12 radiation lengths and an inner ring of 72 $PbWO_4$ crystals of 22.5 radiation lengths at small forward angles. TAPS is normally installed 1.46 m downstream from the target covering polar angles from 5° to 21°. The photon energy resolution is parametrized as $\Delta E/E = 1.8\% + 0.8\%/(E[\text{GeV}])^{0.5}$ [62]. The fine granularity of the detector elements leads to excellent resolution in the polar angle (better than 1°), while $\Delta\phi = 1°$–$6°$. Neutral and charged particles can be discriminated by plastic scintillators in both detectors. A 50 cm long barrel of 24 strips with a width of 4 mm surrounds the target and acts as particle identification detector (PID) for CB [63]. In TAPS charged particles can be identified with individual 5 mm thick plastic scintillators that are installed in front of every detector element. As the dE/E-resolution is worse compared to the PID, alternatively the recently constructed pizza detector could be used. It consists of 24 plastic scintillator sectors and would be place in front of TAPS.

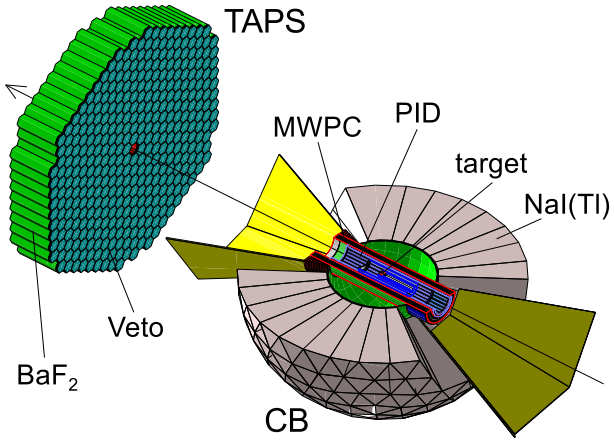

Figure 9: Schematic view of the A2 experimental setup with the central detector Crystal Ball (CB) and the forward calorimeter TAPS, and the corresponding subcomponents for charged particle discrimination (PID, Veto) and tracking (MWPC).

Tests measurements are needed to determine the achievable dE/E-resolution but as the scintillator thickness is 1 cm, it is expected to be rather good [58]. TAPS additionally provides separation of photons and massive particles via time-of-flight measurements and by using the two scintillation light components in the BaF_2 crystals in a pulse-shape analysis.

Although the A2 setup was optimized for the detection of photons, neutrons and charged particles can be detected as well with the following restrictions:

Neutrons Neutrons can be detected in both CB and TAPS with typical efficiencies up to 40%. Separation from photons is only possible in TAPS (time-of-flight, BaF_2 pulse-shape analysis), separation from protons both in TAPS and CB. An energy measurement is not possible since the kinetic energy cannot be deduced from the deposited energy [61].

Protons Protons can be detected in both CB and TAPS with typical efficiencies around 80%. The kinetic energy can be determined from the deposited energy using appropriate corrections up to the punch-through energy (CB: ∼400 MeV, TAPS: ∼380 MeV). Discrimination to pions is possible using the dE/E-technique in CB (up to 250 MeV) and TAPS (up to 150 MeV).

Pions Pions can be detected in both CB and TAPS with typical efficiencies up to 70%. The kinetic energy can be determined from the deposited energy using appropriate corrections up to the punch-through energy (CB: ∼250 MeV, TAPS: ∼200 MeV). The energy resolution for π^--mesons is worse since, once at rest, they will form pionic atoms, which will finally lead to additional energy depositions by emitted protons and photons [64]. Discrimination of charged pions to protons is possible using the dE/E-technique in CB (up to 250 MeV) and TAPS (up to 150 MeV) but the charge of the pions cannot be determined due to the absence of a magnetic field in the setup.

Kaons K^+-mesons can be detected with the in-crystal decay technique [65] in both CB and TAPS with typical efficiencies of 20–30%. If the kinetic energy of the kaons is below

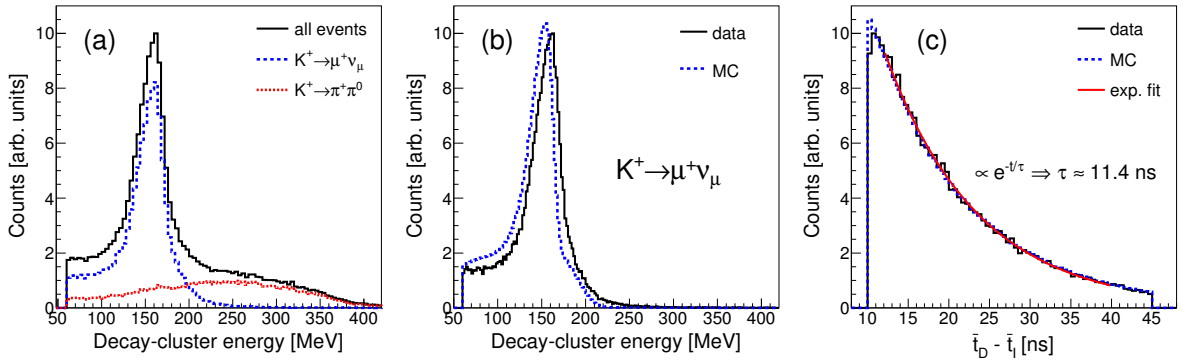

Figure 10: K^+ detection in the Crystal Ball [66]: (a) Energy distribution of the K^+ decay clusters of all events (black solid), pionic decay events (blue dotted) and muonic decay events (red dashed). (b) Comparison of experimental (black solid) and simulated (blue dotted) decay cluster energy distributions for muonic decay events. (c) Impact-decay cluster time difference: Experimental (black solid) and simulated (blue dotted) distributions. Exponential fit to experimental data (red curve).

the punch-through energy (CB: ∼350 MeV, TAPS: ∼330 MeV), they will be stopped in the crystals and decay after a mean lifetime of 12.38 ns [3]. The decay products will deposit additional energy in a secondary cluster connected to the main cluster. An algorithm was developed to search for such cluster signatures [65]. It splits potential K^+-clusters into impact and decay subclusters based on the timing signals. Energy and direction of the kaon can then be accessed via the impact cluster, while properties of the decay cluster help to differentiate between the dominant $\mu^+\nu_\mu$ ($\Gamma_i/\Gamma = 63.56\%$) and $\pi^+\pi^0$ ($\Gamma_i/\Gamma = 20.67\%$) [3] decays.

Fig. 10 shows some characteristic distributions related to the K^+-detection technique. In (a), the decompositon of the total decay cluster energy distribution (black histogram) into the contributions of the muonic (blue histogram) and the pionic (red histogram) decays is illustrated. A clear peak around 150 MeV due to the energy deposited by the μ^+ can be seen, whereas the distribution coming from the pionic decay is broader. Fig. 10(b) shows the good agreement of the experimental and the simulated distributions in case of the muonic decay. Only an overall energy correction is necessary to account for the systematic shift. Finally, the time difference between the impact and the decay cluster is plotted in Fig. 10(c) for experimental and simulated data. As expected, both distributions follow an exponential drop-off and the decay time extracted from the experimental data is in good agreement with the mean lifetime of the K^+-meson [66].

2.2 Kinematics and event reconstruction

The kinematics and event topologies of the signal reactions (R1)–(R4) were studied with simulations based on a Geant4 [67] model of the experimental setup. Events were generated according to the differential cross sections measured by CLAS [24] and using the $\Lambda(1405)$ resonance parameters provided by the PDG [3]. The resulting lab polar angles and kinetic energies of all final state particles for the proposed A2 experiment are shown in Fig. 11. For all reactions, most of the kaons will be going to TAPS with kinetic energies mostly below the punch-through limit, so that a clean detection via the in-crystal decay technique is possible. The kinematics is similar for protons coming from the Λ-decay. Time-of-flight,

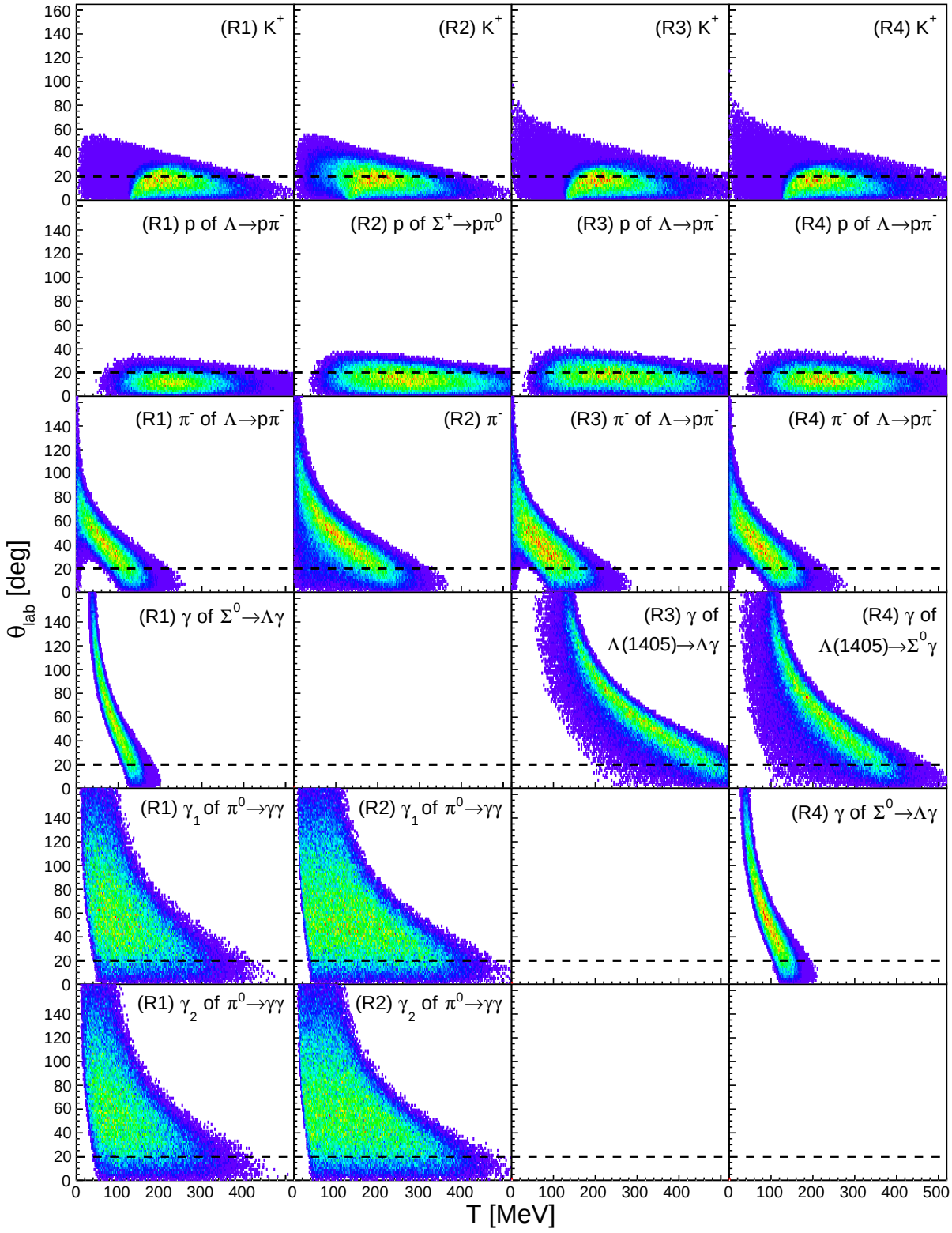

Figure 11: Kinematics of $\gamma p \to K^+\Lambda(1405)$ in a simulation of the proposed A2 experiment. $\Lambda(1405)$ decays in columns, particles in rows: (R1) $\Lambda(1405) \to \Sigma^0\pi^0$, (R2) $\Lambda(1405) \to \Sigma^+\pi^-$, (R3) $\Lambda(1405) \to \Lambda\gamma$, (R4) $\Lambda(1405) \to \Sigma^0\gamma$. The dashed line represents the CB-TAPS transition.

dE/E and the BaF_2 pulse-shape analysis techniques will further help to achieve a clean identification of those particles in TAPS. The pions originating from the decay of the Λ are mainly going to CB. Their energies are in the region were a clean separation from protons via dE/E is possible. This will be more difficult for pions in TAPS since their energies are higher and the dE/E resolution is worse using the TAPS vetos. Alternatively, one could use the still to be tested pizza detector. The MWPC could be used to reconstruct the pion tracks but as the majority of protons will be detected in TAPS, where no tracking is available, the exact determination of the Λ-decay vertex will not be possible anyway. Regarding the photons coming from the decays of the hyperons and the π^0, there will be no issues at all. Most of them are going to CB, where they will contribute to the energy sum trigger.

The event reconstruction is requiring the detection of the complete final state. The final analysis will exploit all possibilities for particle identification provided by the different detectors. In the preliminary analyses presented here, the following selection criteria were applied:

- detection of K^+ cluster candidate via the subcluster finder algorithm, hit in PID or TAPS veto required. Only the $K^+ \to \mu^+\nu_\mu$ is considered in this test analysis.
- identification of π^- and proton via dE/E in CB (PID) and TAPS (vetos)
- identification of photons via PID and veto detectors (no hit requested)

A kinematic fit [68] of the corresponding signal reaction was performed on all particle combinations fulfilling these criteria and the solution yielding the lowest χ^2 was used in the subsequent analysis steps. Depending on the signal reaction, further cuts were applied to obtain the results shown in the following:

- 3σ-cut (CL $< 2.7 \times 10^{-3}$) on the confidence level of the best kinematic fit
- 3σ-cut on $m(\gamma\gamma)$ to select π^0-mesons or to exclude them
- 3σ-cut on the rest frame energy E_γ^{rest} of the Σ^0 decay photon
- 3σ-cuts on the differences of the detected and calculated proton polar and azimuthal angles

Furthermore, the simulated events were subject to a realistic model of the A2 trigger consisting of an energy sum threshold for the Crystal Ball detector and a multiplicity condition of logical units in CB and TAPS. The units in CB are made from 45 sectors each containing up to 16 neighboring crystals, while 6 triangular sectors are constituting the units in TAPS. In both detectors, one crystal per unit exceeding the corresponding threshold will mark the unit as hit. A condition is then applied on the number of hit units which roughly corresponds to the number of detected particle clusters (not taking into account multiple clusters in a single unit or a single cluster spreading over several units).

The final resolutions of the $\Sigma^0\pi^0$ and $\Sigma^+\pi^-$ invariant mass distributions in the region of interest are shown in Figs. 12(a) and 13(a). They were obtained by simulating events with $m(\Sigma\pi) = 1.405$ GeV (zero intrinsic width). Two different experimental scenarios were considered. In the first case, a 4 mm photon beam collimator and a 10 cm long target cell was used. This corresponds to the experimental setup of the 2014 η'-experiment. In

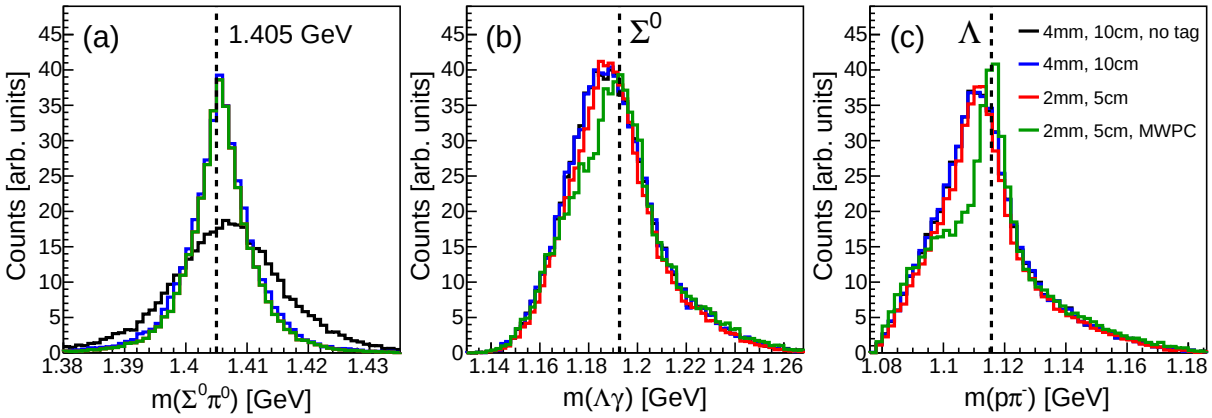

Figure 12: Resolutions at $m(\Sigma\pi) = 1.405$ GeV in the $\Lambda(1405) \rightarrow \Sigma^0\pi^0$ analysis: (a) final $\Sigma^0\pi^0$ invariant mass showing the $\Lambda(1405)$ resolution. (b) $\Lambda\gamma$ invariant mass showing the Σ^0 signal. (c) $p\pi^-$ invariant mass showing the Λ signal. The colors of the histograms denote different experimental conditions and event reconstruction techniques (see text).

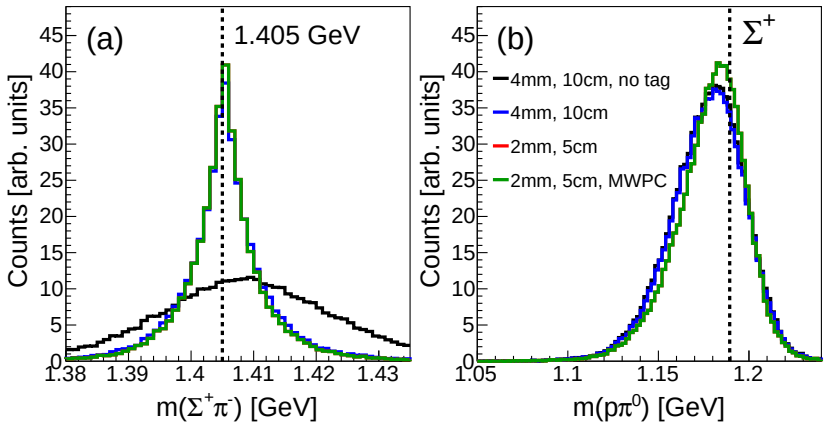

Figure 13: Resolutions at $m(\Sigma\pi) = 1.405$ GeV in the $\Lambda(1405) \rightarrow \Sigma^+\pi^-$ analysis: (a) final $\Sigma^+\pi^-$ invariant mass showing the $\Lambda(1405)$ resolution. (b) $p\pi^0$ invariant mass showing the Σ^+ signal. The colors of the histograms denote different experimental conditions and event reconstruction techniques (see text).

the second case, a 2 mm collimator and a 5 cm target was tested. The motivation for these settings was mainly to investigate if a spatially more restricted primary vertex would improve the final $m(\Sigma\pi)$ resolutions. This seems not to be the case. Furthermore, the effect of using the MWPC for the track reconstruction of the charged particles was explored. Only a minor improvement in the $m(\Sigma\pi)$ distributions can be observed. Approximated Gaussian FWHM resolutions in both the $\Sigma^0\pi^0$ and $\Sigma^+\pi^-$ invariant masses of 10 MeV are observed. Finally, the scenario of running an untagged experiment, i.e., without using the information of the photon tagger, was tested. The advantage of running untagged would be potentially higher beam currents. But, since in this case the beam photon energy has an uncertainty of $\sim$78 MeV, the resulting $\Sigma^0\pi^0$ and $\Sigma^+\pi^-$ resolutions are twice and three times worse, respectively, than when running with the tagger.

Figs. 12(b),(c) and 13(b) show the signal distributions of the different intermediate hyperons of the two $\Sigma\pi$ analysis channels. Again, only a minor improvement of the more restricted primary vertex setup can be seen. The use of the MWPC gives the most notable

improvement in terms of signal width and position for the Λ-reconstruction, which then improves also slightly the Σ^0-signal. On the other hand, the reconstruction of the more short-lived Σ^+ seems not to profit significantly. As the calculations of the shown hyperon distributions are not using the photon tagger information, the untagged scenario does not yield different distributions.

2.3 Detection efficiencies and background contamination

The detection efficiencies of reactions (R1)–(R4) were determined with simulations of the standard experimental setup using a 4 mm photon beam collimator and a 10 cm long target cell (equivalent to the 2014 η'-experiment). The main questions to be addressed in this section is the optimal choice of the experimental trigger and the amount of background contamination in all analyses channels.

Different thresholds in the range of 100–550 MeV for the energy sum trigger in CB were investigated. A trigger multiplicity of 4 and higher (M4+) was used along with all energy sum thresholds with the exception of the 550 MeV setting, in which no multiplicity condition was applied to reproduce the trigger of the 2014 η'-experiment. The M4+ multiplicity condition denotes the highest reasonable multiplicity sensitive for reactions (R1)–(R4), where at least four particles need to be detected, while rejecting large parts of events having less than four final state particles. The use of M4+ is motivated by the findings discussed in the following. Namely, it was found that a low CB energy sum threshold increases the detection efficiencies for all reactions of interest. On the other hand, a low threshold will let pass a large number of unwanted events with higher production cross sections, possibly saturating the data acquisition system. Therefore, the multiplicity condition should be as restrictive as possible. As most particles of reactions (R1)–(R4) going to TAPS have kinetic energies above 80 MeV, the threshold for the multiplicity sectors in TAPS were set to this value to simulate optimized settings concerning background rejection. The threshold for the CB units were left at the standard value of 30 MeV.

Different sources of possible background contributions were checked in the analyses of the signal reactions (R1)–(R4). They can be divided into four groups that will be briefly discussed in the next paragraphs. More specific comments concerning the background contamination in each of the signal reactions will be given afterwards.

Nonstrange background Nonstrange reactions, such as $\gamma p \to p\pi^+\pi^-\pi^0$ (also resonant via η/ω-photoproduction), $\gamma p \to p\eta\pi^0$, and $\gamma p \to p\omega\pi^0$ with $\eta/\omega \to \pi^+\pi^-\pi^0$ could mock the signal final states because $\pi^\pm$ (and also neutrons) can be marked as kaons by the in-crystal decay detection algorithm. The probability for this to happen is very small so that in general the K^+-tag given by the algorithm provides a very characteristic signature for strangeness photoproduction events. Nevertheless, as the nonstrange cross sections are much higher than the one for the $\Lambda(1405)$-production, possible contamination from these channels was investigated. It was found that only a negligible amount of events pass the particle number and type selection criteria, hence it is expected that other reactions yielding the same (or different by ± 1 photon) final states are also very unlikely to contribute significantly. The application of the further analysis cuts discussed in Sec. 2.2 completely removed all nonstrange background events in all four analyses.

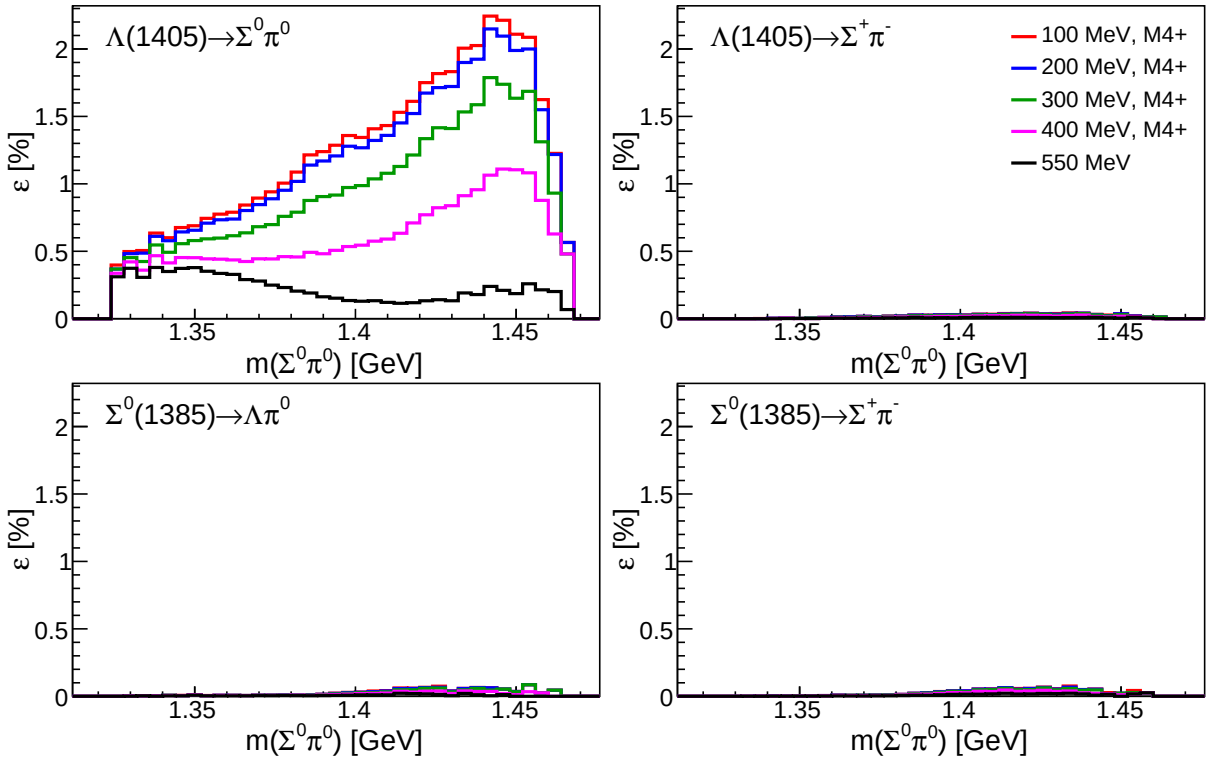

Figure 14: Detection efficiencies of signal (top left) and $\Lambda(1405)/\Sigma^0(1385)$ hadronic decay background contributions in the $\Lambda(1405) \to \Sigma^0\pi^0$ analysis as a function of the $\Sigma^0\pi^0$ invariant mass.

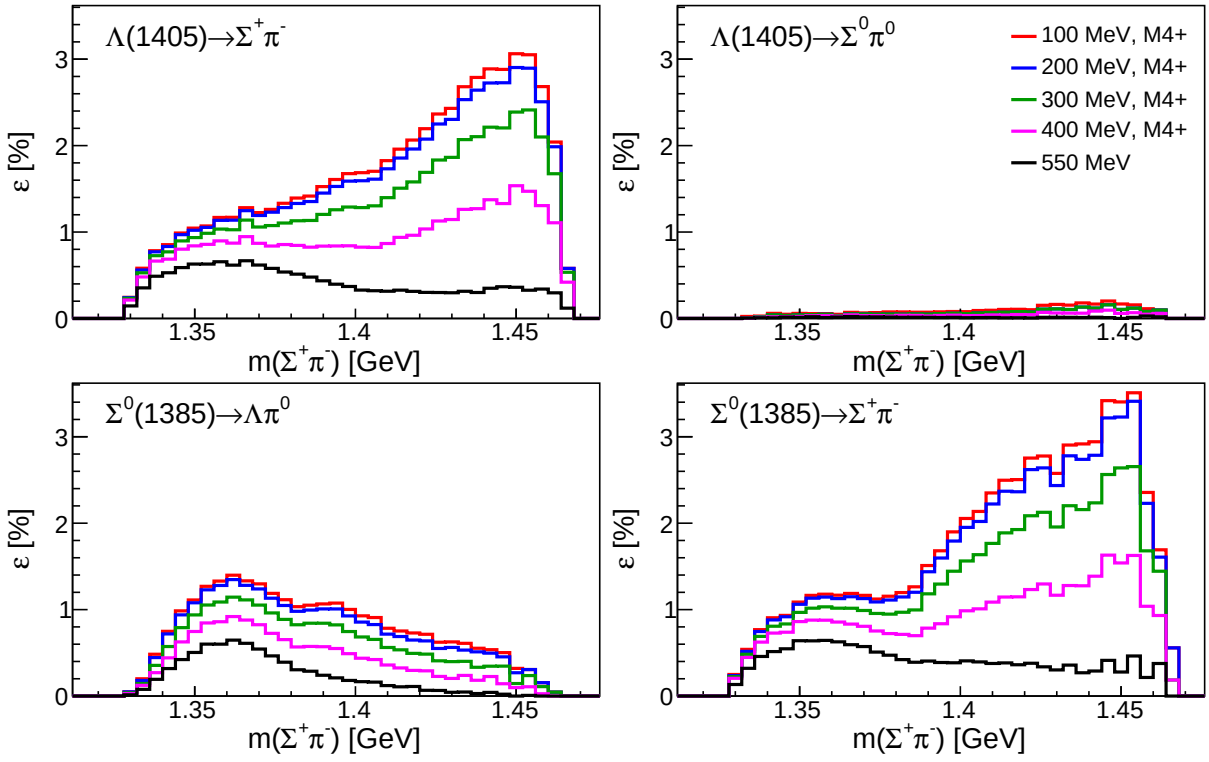

Figure 15: Detection efficiencies of signal (top left) and $\Lambda(1405)/\Sigma^0(1385)$ hadronic decay background contributions in the $\Lambda(1405) \to \Sigma^+\pi^-$ analysis as a function of the $\Sigma^+\pi^-$ invariant mass.

Ground-state hyperon production The reactions $\gamma p \to K^+\Lambda$ and $\gamma p \to K^+\Sigma^0$ have roughly 10 times higher cross sections than $\gamma p \to K^+\Lambda(1405)$ and could contaminate the signal reactions due to the presence of the kaon. Especially reaction (R3) could be affected since it has exactly the same final state as Σ^0-production. Indeed, a notable contamination was found in the analysis of simulated data but since the $\Lambda(1405)$ and the Σ^0 decay photons have different energies, the removal of this background channel is straightforward and can be done by a simple cut. No contamination was found for the other reactions.

$\Sigma^0(1385)$-production The cross section of $\gamma p \to K^+\Sigma^0(1385)$ is almost 3 times higher than the $\Lambda(1405)$-production cross section in the region covered by this experiment. In addition, some of the decays (see Tab. 1) lead to the same final states as in the $\Lambda(1405)$ signal reactions. While (R1) is not affected in first order due to $\Sigma^0(1385) \not\to \Sigma^0\pi^0$ (isospin forbidden), (R2) will see some contributions from $\Sigma^0(1385) \to \Sigma^+\pi^-$. As the radiative decays of the $\Sigma^0(1385)$ and the $\Lambda(1405)$ yield exactly the same final states, contamination is inevitable for (R3) and (R4) and a simultaneous analysis for the two hyperons needs to be performed.

Mutual contamination of signal reactions Because of the equal or similar final states of the signal reactions (R1)–(R4), also mutual contamination is possible and needs to be investigated. Contamination of the hadronic $\Lambda(1405)$-decays by the radiative decays can of course be neglected due to the tiny branching ratios of the latter, while contamination into the other direction could be substantial.

The detection efficiencies of signal and background reactions in the $\Lambda(1405) \to \Sigma^0\pi^0$ analysis (R1) are plotted in Fig. 14 as a function of the $\Sigma^0\pi^0$ invariant mass. As mentioned before, different CB energy sum trigger thresholds were simulated and the corresponding efficiencies are shown by curves of different color. The average signal efficiencies (top left) range from 0.23% (550 MeV sum trigger) to 1.25% (100 MeV, M4+). The factor of $\sim$5.4 between these two extreme cases illustrates the strong influence of the energy sum trigger, especially for higher values of $m(\Sigma^0\pi^0)$, where most kaons are going to TAPS and cannot contribute to the deposited energy in CB. For lower values of $m(\Sigma^0\pi^0)$ the efficiency is generally lower because there are more high-energy undetected kaons punching-through the detectors. As shown in the other plots of Fig. 14, the efficiency for the considered background channels is only a few percent with respect to the signal efficiency. Nevertheless, considering all factors a contamination of $\sim$17% coming from $\Sigma^0(1385) \to \Lambda\pi^0$ must be expected in the worst case (see Tab. 2).

The detection efficiencies of signal and background reactions in the $\Lambda(1405) \to \Sigma^+\pi^-$ analysis (R2) are plotted in Fig. 15 as a function of the $\Sigma^+\pi^-$ invariant mass. The average signal efficiencies (top left) range from 0.41% (550 MeV sum trigger) to 1.70% (100 MeV, M4+) and are thus significantly higher than for (R1). This is probably mostly due to the lower multiplicity final state and the less distant secondary vertex of the Σ^+-hyperon. The efficiency of the $\Sigma^0(1385) \to \Sigma^+\pi^-$ background reaction is even slightly higher than for the signal reaction, while the efficiency of $\Sigma^0(1385) \to \Lambda\pi^0$, which leads to the exactly same final state, is considerably lower. The efficiency of the $\Lambda(1405) \to \Sigma^0\pi^0$ decay is very small. Taken into account all factors (see Tab. 2), the $\Sigma^0(1385) \to \Lambda\pi^0$ seems to give a major contribution roughly more than four times stronger than the signal. The simple analysis

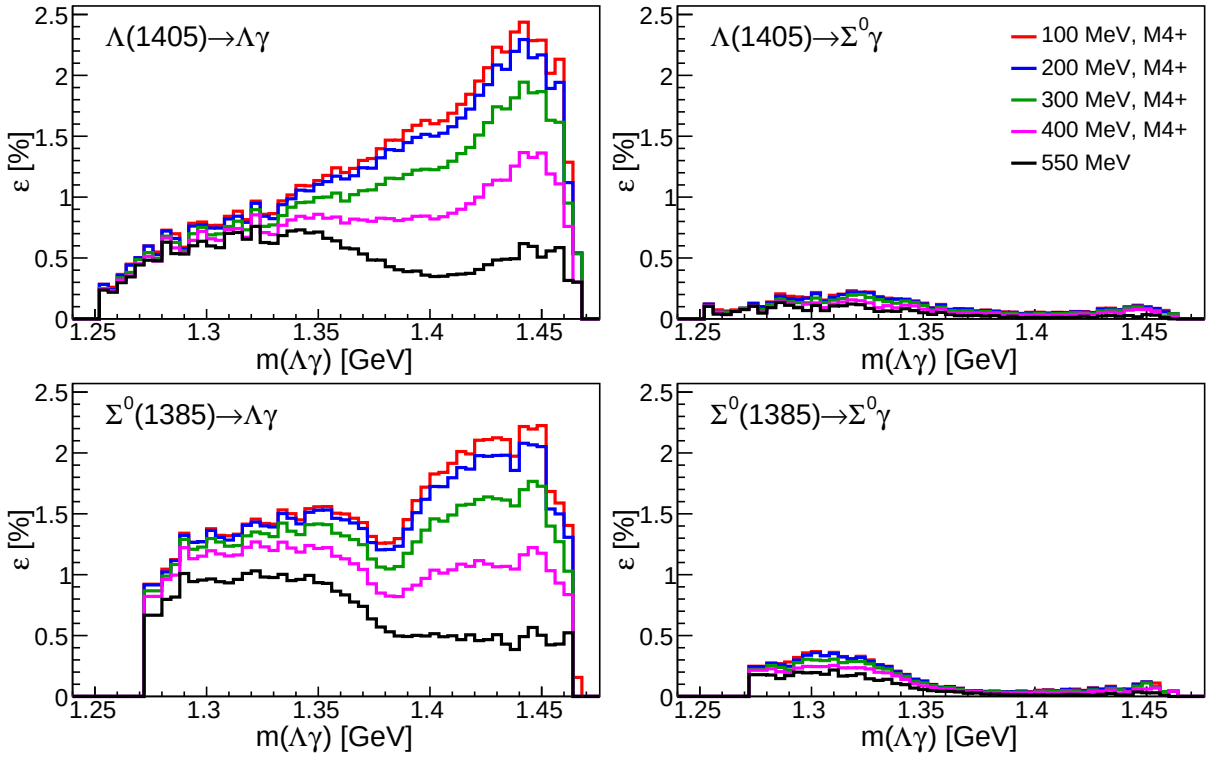

Figure 16: Detection efficiencies of signal (top left) and $\Lambda(1405)/\Sigma^0(1385)$ radiative decay background contributions in the $\Lambda(1405) \rightarrow \Lambda\gamma$ analysis as a function of the $\Lambda\gamma$ invariant mass.

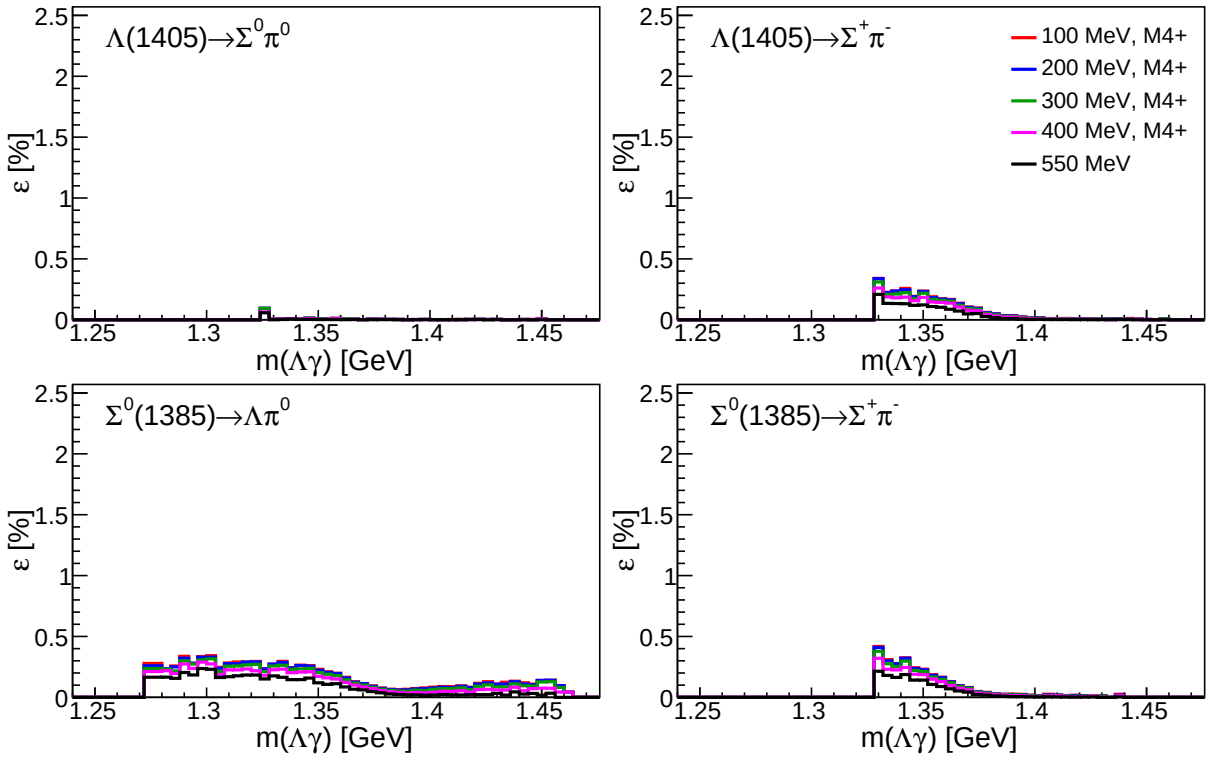

Figure 17: Detection efficiencies of the $\Lambda(1405)/\Sigma^0(1385)$ hadronic decay background contributions in the $\Lambda(1405) \rightarrow \Lambda\gamma$ analysis as a function of the $\Lambda\gamma$ invariant mass.

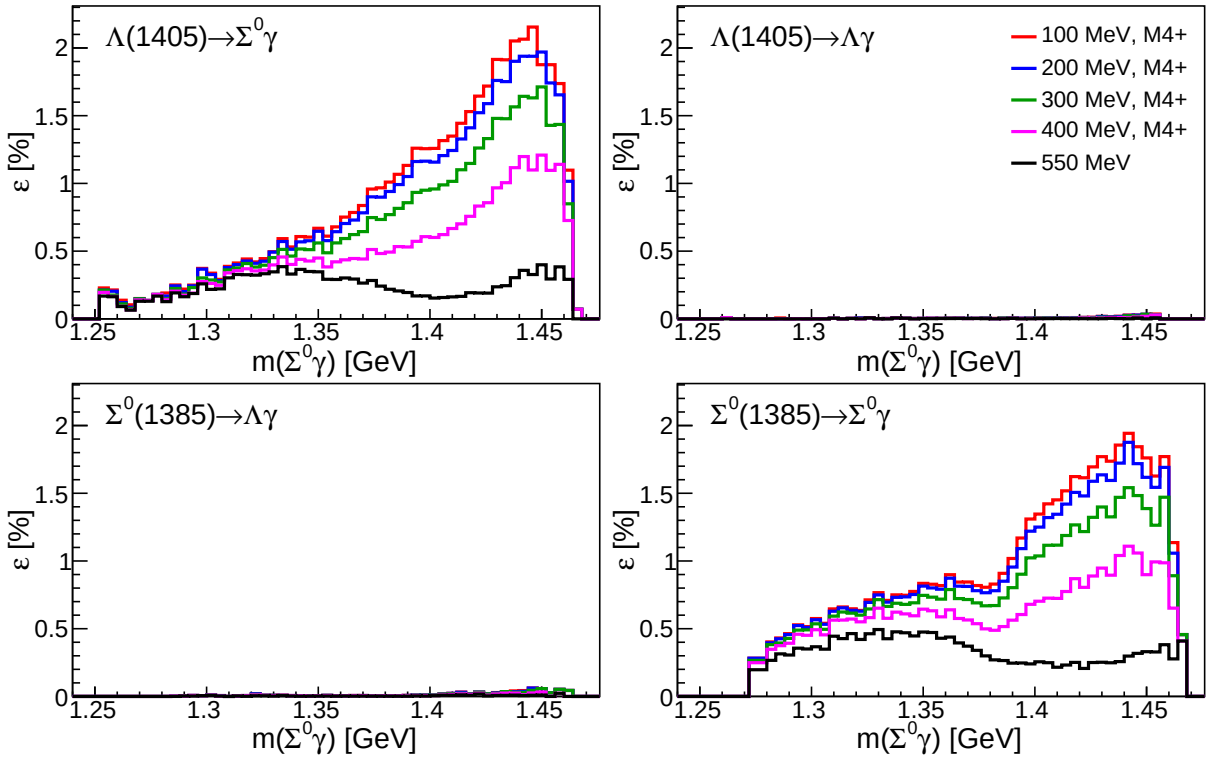

Figure 18: Detection efficiencies of signal (top left) and $\Lambda(1405)/\Sigma^0(1385)$ radiative decay background contributions in the $\Lambda(1405) \to \Sigma^0\gamma$ analysis as a function of the $\Sigma^0\gamma$ invariant mass.

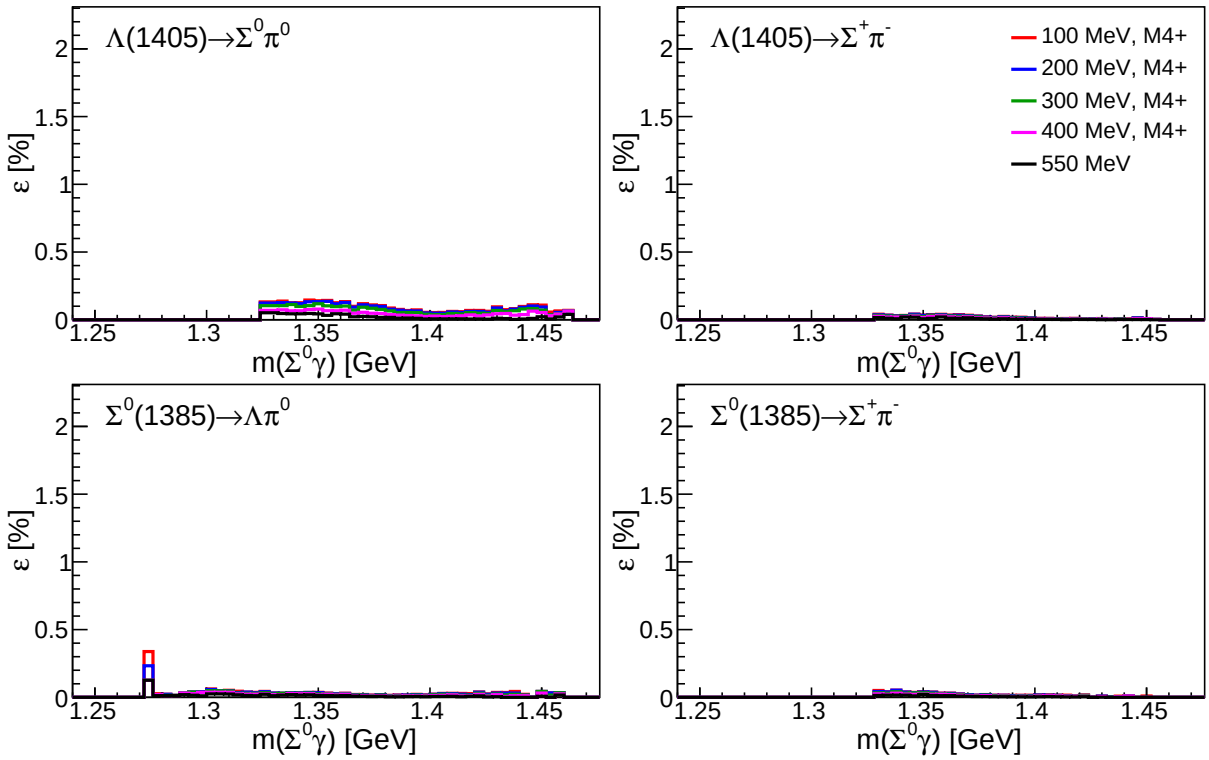

Figure 19: Detection efficiencies of the $\Lambda(1405)/\Sigma^0(1385)$ hadronic decay background contributions in the $\Lambda(1405) \to \Sigma^0\gamma$ analysis as a function of the $\Sigma^0\gamma$ invariant mass.

performed for this work is therefore not sufficient for the signal extraction and some better methods need to be applied in the final analysis. Once the background contributions will have been suppressed sufficiently, a separation of the different channels should be possible for example by fitting the different $m(\Sigma^+\pi^-)$ distributions (see Fig. 21) to the experimental spectrum.

The detection efficiencies of signal and background reactions in the $\Lambda(1405) \rightarrow \Lambda\gamma$ analysis (R3) are plotted in Figs. 16 and 17 as a function of the $\Lambda\gamma$ invariant mass. Here possible contamination from all hadronic (with the exception of $\Sigma^-\pi^+$) and radiative decays of the $\Lambda(1405)$ and the $\Sigma^0(1385)$ were considered. The average signal efficiencies (top left of Fig. 16) range from 0.51% (550 MeV sum trigger) to 1.25% (100 MeV, M4+). Due to the high energetic $\Lambda(1405)$ decay photon contributing to the CB energy sum, the efficiency for low values of $m(\Lambda\gamma)$, where also more kaons are detected in CB, is almost the same for all energy sum thresholds. Obviously the $\Sigma^0(1385) \rightarrow \Lambda\gamma$ decay has a equally high efficiency, while the radiative decays of both excited hyperons to the $\Sigma^0\gamma$ final state are much small although still notable. On the same low level are the contaminations from the hadronic decays shown in Fig. 17 with the exception of the $\Lambda(1405) \rightarrow \Sigma^0\pi^0$ channel, which is even more suppressed. According to Tab. 2 the $\Sigma^0(1385) \rightarrow \Lambda\pi^0$ will be the dominant background in this analysis but basically all final states except $\Lambda(1405) \rightarrow \Sigma^0\gamma$ will contaminate the signal. It has to be stressed again that the performed analysis was rather simple and only exploited a limited number of cuts. Surely the different distributions of all contributions in, e.g., the $\Lambda\gamma$ invariant mass (Fig. 22) or the $\Lambda(1405)$ decay photon energy in the $\Lambda(1405)$ rest frame (Fig. 23) will be useful for disentangling the various channels in a more elaborate analysis.

The detection efficiencies of signal and background reactions in the $\Lambda(1405) \rightarrow \Sigma^0\gamma$ analysis (R4) are plotted in Figs. 18 and 19 as a function of the $\Sigma^0\gamma$ invariant mass. As before, possible contamination from all hadronic and radiative decays of the $\Lambda(1405)$ and the $\Sigma^0(1385)$ were considered. The average signal efficiencies (top left of Fig. 18) range from 0.25% (550 MeV sum trigger) to 0.87% (100 MeV, M4+). Again, the corresponding radiative decay of the $\Sigma^0(1385)$ has an equally high efficiency. The other radiative decays only have very low efficiencies. Efficiencies of the hadronic decays of both hyperons are low but because of the high production cross section and branching ratio, the $\Sigma^0(1385) \rightarrow \Lambda\pi^0$ decay will be the dominant background again (see Tab. 2). The separation of this and all other backgrounds will make use of the different $\Lambda\gamma$ invariant mass and $\Lambda(1405)$ decay photon energy distributions shown in Fig. 24 and Fig. 25, respectively.

2.4 Extraction of observables and cross checks

An estimation of the to be expected effective strengths of the signal and background contributions is shown in Tab. 2. The detection efficiencies correspond to the 200 MeV CB energy sum, M4+ trigger scenario. The branching ratios for the hadronic decays were taken from Tab. 1. The radiative decay widths suffer from considerable uncertainties caused by the large range of theoretical values and the absence of a previous direct measurement (see Sec. 1.4). We motivate our choice by the most recent results from unitary chiral theory (see Eqns. 6 and 7) and use an average value for both decays of $\Gamma_{Y\gamma} = 70$ keV for all further calculations. This is also close to the overall average of the model calculations shown in Tab. I of Ref. [40]. The assumed branching ratios are thus $\Gamma_{\Lambda\gamma}/\Gamma = \Gamma_{\Sigma^0\gamma}/\Gamma = 1.39 \times 10^{-3}$. Also, the unknown $\Gamma_{\Sigma^0\gamma}/\Gamma$ for the $\Sigma^0(1385)$ was assumed to be equal to $\Gamma_{\Lambda\gamma}/\Gamma = 1.25 \times 10^{-2}$.

	ϵ_{det} [%]	$\Gamma_i/\Gamma\,(Y^*)$	$\Gamma_i/\Gamma\,(Y)$	σ [nb]	c_{eff}
(R1) $\Lambda(1405)\rightarrow \Sigma^0\pi^0$					
signal	1.19	33%	64%	154	1.00
$\Lambda(1405)\rightarrow \Sigma^+\pi^-$	0.02	33%	52%	154	0.01
$\Sigma^0(1385)\rightarrow \Lambda\pi^0$	0.03	87%	64%	404	0.17
$\Sigma^0(1385)\rightarrow \Sigma^+\pi^-$	0.03	6%	52%	404	0.01
(R2) $\Lambda(1405)\rightarrow \Sigma^+\pi^-$					
signal	1.62	33%	52%	154	1.00
$\Lambda(1405)\rightarrow \Sigma^0\pi^0$	0.07	33%	64%	154	0.05
$\Sigma^0(1385)\rightarrow \Lambda\pi^0$	0.74	87%	64%	404	3.89
$\Sigma^0(1385)\rightarrow \Sigma^+\pi^-$	1.73	6%	52%	404	0.51
(R3) $\Lambda(1405)\rightarrow \Lambda\gamma$					
signal	1.18	1.39×10^{-3}	64%	154	1.00
$\Lambda(1405)\rightarrow \Sigma^0\gamma$	0.11	1.39×10^{-3}	64%	154	0.09
$\Sigma^0(1385)\rightarrow \Lambda\gamma$	1.50	1.25×10^{-2}	64%	404	29.99
$\Sigma^0(1385)\rightarrow \Sigma^0\gamma$	0.15	1.25×10^{-2}	64%	404	3.00
$\Lambda(1405)\rightarrow \Sigma^0\pi^0$	0.01	33%	64%	154	2.01
$\Lambda(1405)\rightarrow \Sigma^+\pi^-$	0.08	33%	52%	154	13.08
$\Sigma^0(1385)\rightarrow \Lambda\pi^0$	0.17	87%	64%	404	236.55
$\Sigma^0(1385)\rightarrow \Sigma^+\pi^-$	0.10	6%	52%	404	7.80
(R4) $\Lambda(1405)\rightarrow \Sigma^0\gamma$					
signal	0.82	1.39×10^{-3}	64%	154	1.00
$\Lambda(1405)\rightarrow \Lambda\gamma$	0.01	1.39×10^{-3}	64%	154	0.01
$\Sigma^0(1385)\rightarrow \Lambda\gamma$	0.02	1.25×10^{-2}	64%	404	0.58
$\Sigma^0(1385)\rightarrow \Sigma^0\gamma$	0.96	1.25×10^{-2}	64%	404	27.62
$\Lambda(1405)\rightarrow \Sigma^0\pi^0$	0.09	33%	64%	154	26.06
$\Lambda(1405)\rightarrow \Sigma^+\pi^-$	0.02	33%	52%	154	4.70
$\Sigma^0(1385)\rightarrow \Lambda\pi^0$	0.03	87%	64%	404	60.07
$\Sigma^0(1385)\rightarrow \Sigma^+\pi^-$	0.02	6%	52%	404	2.24

Table 2: Estimation of effective contributions c_{eff} for the 200 MeV CB energy sum, M4+ trigger scenario based on detection efficiencies ϵ_{det}, branching ratios Γ_i/Γ for the excited hyperon $Y^* = \{\Lambda(1405), \Sigma^0(1385)\}$ and the secondary hyperon $Y = \{\Lambda, \Sigma^0\}$, and the production cross sections σ.

The production cross sections for the $\Lambda(1405)$ and the $\Sigma^0(1385)$ were estimated from the CLAS measurements [24] by linear interpolation from the corresponding reaction threshold to the first data point at $E_\gamma = 1662$ MeV. An average cross section in the photon beam energy range covered by the endpoint tagger was then calculated. Finally, the effective contributions were normalized to the signal contribution.

In all analysis channels, the $\Sigma^0(1385)\rightarrow \Lambda\pi^0$ contribution seems to be the largest background. As can be seen in Figs. 21–25, a separation using the shown variables (amongst others) should be possible with techniques such as sPlot [69], but as the magnitude of the background is rather large, a better rejection needs to be implemented beforehand using more sophisticated analysis methods. For example, an optimization of the signal-to-

background ratios based on the confidence levels of kinematic fits of all reactions candidates could be implemented. This approach was already successfully used in the measurement of the $\Sigma^0(1385) \rightarrow \Lambda\gamma$ decay width [47].

The following list summarizes several cross checks that can be performed in the proposed experiment, and some additional advantages:

- The second Λ-decay $\Lambda \rightarrow n\pi^0$ provides an independent data set (with lower statistics) with a completely different final state and detection efficiencies.
- The radiative decays of the $\Sigma^0(1385)$ will have to be extracted in parallel and the obtained result for $\Gamma_{\Lambda\gamma}$ can be compared to the previously measured value [40, 47].
- The flux normalization can be checked via the determination of the photoproduction cross sections for the $\Sigma^0(1385)$ or nonstrange mesons.
- Absolute normalization is only needed for the $(\Sigma\pi)^0$ line-shape observables.
- Systematic uncertainties due to detection efficiencies will be small in the extraction of the beam-helicity asymmetry $I^{\odot}$ and the radiative decay widths because of cancellation effects.

2.5 Running conditions

Due to the small $\Lambda(1405)$-production cross sections, the proposed experiment should run at the highest possible luminosity. This includes the use of a 4mm collimator and a 10 cm long hydrogen target. As discussed in Sec. 2.2, the benefits of a smaller beam spot and a shorter target would only be marginal, but on the other hand lead to a decrease in luminosity by $\sim$75%. Even higher luminosities would be possible in an untagged experiment but this would reduce the photon beam energy resolution dramatically, which would lead to unacceptable resolutions in the observables and to severe difficulties in the background rejection. Unfortunately, high luminosities make the use of the MWPC impossible due to rate limitations, but, as shown in Sec. 2.2, no substantial advantage enabled by their use could be observed in the event reconstruction.

Test measurements using a 4mm collimator and a 10 cm long hydrogen target but varying other experimental parameters were performed in July 2014 in preparation of the η'-experiment. Those measurements allow a more accurate estimation of the parameters for the proposed experiment. The detection efficiencies presented in Sec. 2.3 suggest that a 200 MeV CB energy sum, M4+ trigger seems to be a reasonable trigger setting. Test data using a 250 MeV CB energy sum threshold without multiplicity condition is available [70] and shows the following distribution of multiplicities: M1 (10%), M2 (30%), M3 (40%), M4+ (20%). Hence, we deduce that applying the M4+ multiplicity condition could reduce the trigger rate by up to a factor of 5 when using a 200 MeV CB energy sum threshold. This would allow to increase the beam current by a factor of up to 5 compared to the test measurement yielding 5×14 nA = 70 nA at a data acquisition livetime of $\sim$60%. This is close to the beam current used during production running of the η'-experiment (60 nA) and still well below the hardware limit of the endpoint tagger (110 nA). A further increase of the beam current towards this limit is only possible when the trigger rate is reduced even more. Requiring a hit in the endpoint tagger for a positive trigger decision would be an option to be tested for the proposed experiment. For the η'-decays experiment in 2014,

this mechanism was found to be not useful since at 30 nA, a trigger reduction of only 10% could be achieved [71]. Nevertheless, this depends on the main trigger settings and the benefit of having the EPT contributing to the trigger decision is expected to be higher for lower CB energy sum thresholds. Namely, a reduction of the tagged event ratio from 11% to 5% was observed when the energy sum threshold was lowered from 550 MeV to 250 MeV. Other options enabling even higher beam currents would be a threshold Čerenkov detector vetoing electrons and pions, or an FPGA-based kaon trigger in TAPS sensitive to the in-crystal decays.

Smaller changes to the standard experimental settings that could further optimize the signal detection efficiencies and the background suppression, would be checked in detail before the experiment. They include the use of the pizza detector as dE and time-of-flight detector for TAPS, the position of this detector and TAPS with respect to the target, the closing of the backward hole in CB with spare BaF_2 crystals or thick plastic scintillator veto detectors, and the use of a cylindrical PID detector inside CB with a larger radius in place of the unusable MWPC.

2.6 Combination with other experiments

Combined running with another experiment is possible by, e.g., changing the trigger conditions on a regular basis during the experiment or by trigger prescaling. This could even be helpful for obtaining data with a less restrictive trigger conditions for calibration purposes. The proposed trigger for this experiment combined with the higher-lying tagged photon energy range could make the $a_0(980)/f_0(980)$ scalar meson production experiment (LOI to the PAC 2013 [72]) possible on hydrogen. If this experiment would be performed using a deuterium target, we could consider measuring a part of our proposed experiment (radiative decays) on that target as well. Finally, certain decays of the η' and ω-mesons studied in the ongoing analyses of the 2014 endpoint-tagger data could benefit from additional data provided by the complementary trigger of our experiment.

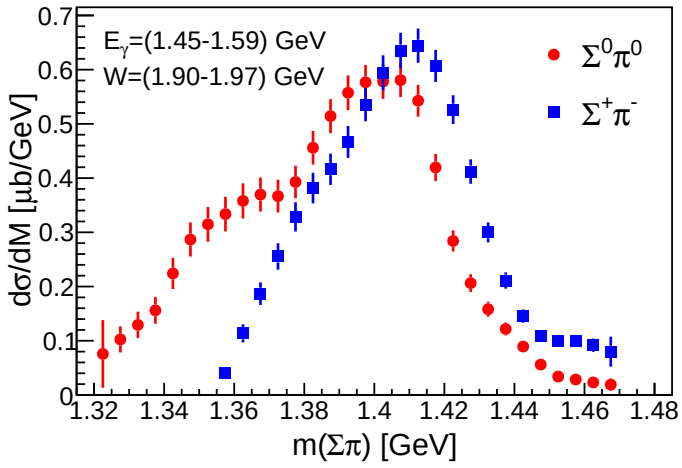

Figure 20: Expected statistical quality of the $\Lambda(1405)$ $(\Sigma\pi)^0$ line shapes obtained in the proposed experiment.

3 Beamtime request

The beamtime request is made based on the measurement of the $\Lambda(1405) \rightarrow \Sigma^0\gamma$ radiative decay width with a statistical uncertainty of 25%. This corresponds to the uncertainty of the first measurement of the $\Sigma^0(1385) \rightarrow \Lambda\gamma$ decay width [40]. Realistic numbers for the $\Lambda(1405) \rightarrow \Lambda\gamma$ will be very similar after a more extended background subtraction, hence a common calculation can be performed using the formula

$$\Delta t = \left[\delta_{stat}^2 \cdot \sigma \cdot N_{e^-} \cdot \epsilon_{tag} \cdot \rho_t \cdot \epsilon_{det} \cdot \epsilon_{daq} \cdot \Gamma_i/\Gamma\right]^{-1} \tag{8}$$

and the corresponding values for the tagged photon energy range E_γ =1450–1590 MeV

σ	production cross section	154 nb
N_{e^-}	detected electrons	2.76×10^7 s^{-1} at 70 nA
ϵ_{tag}	tagging efficiency	60%
ρ_t	target density	0.4215 b^{-1} (10 cm LH_2)
ϵ_{det}	detection efficiency	0.90%
ϵ_{daq}	DAQ livetime	60%
Γ_i/Γ	branching ratio	$1.39 \times 10^{-3} \cdot 64\% \cdot 84\%$
δ_{stat}	relative statistical uncertainty	25%

where the additional branching ratio of 84% comes from the sum of the two analyzable K^+-decays ($\Gamma_{\mu^+\nu_\mu}/\Gamma = 63.56\%$, $\Gamma_{\pi^+\pi^0}/\Gamma = 20.67\%$) and ϵ_{det} is the weighted average detection efficiency for the two kaon-decay analyses. In addition to the $\Delta t \approx 1000$ hours of production running, we ask for an additional block of 150 hours for setting up and optimizing the experiment and request thus a total beamtime of

1150 hours.

The corresponding projected results for the $(\Sigma\pi)^0$ line shapes are shown in Fig. 20.

Acknowledgements

D.W. acknowledges support by the Schweizerischer Nationalfonds (158822, 167759).

A Additional figures

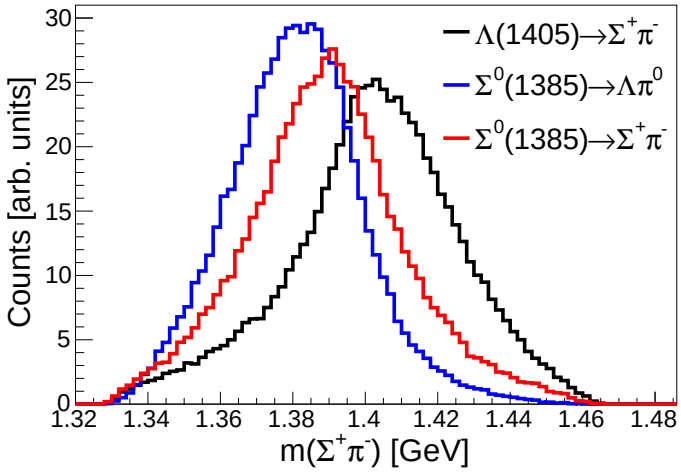

Figure 21: $m(\Sigma^+\pi^-)$ distributions (arb. scaling) in the $\Lambda(1405) \to \Sigma^+\pi^-$ analysis for the signal (black curve) and the two most important background contributions (blue and red curves).

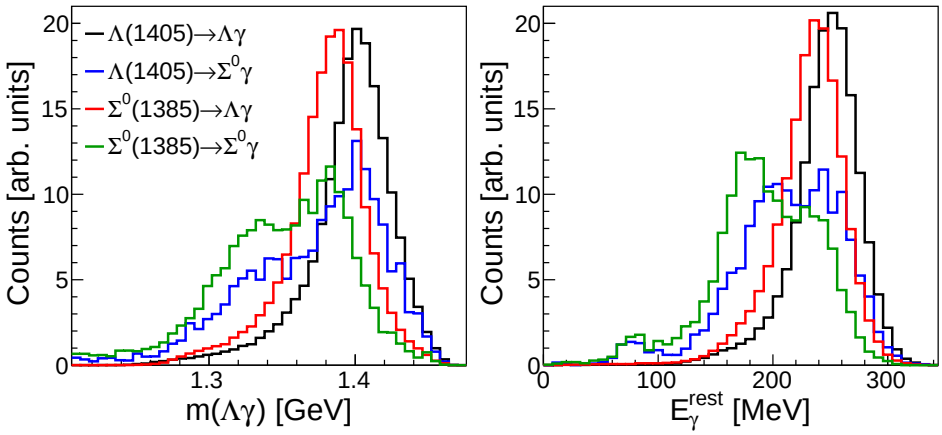

Figure 22: Left side: $m(\Lambda\gamma)$ distributions (arb. scaling) in the $\Lambda(1405) \to \Lambda\gamma$ analysis for the signal (black curve) and the background caused by the other $\Lambda(1405)/\Sigma^0(1385)$ radiative decays (blue, red and green curves). Right side: Corresponding distributions of the $\Lambda(1405)$ decay photon energy ($\Lambda(1405)$ rest frame).

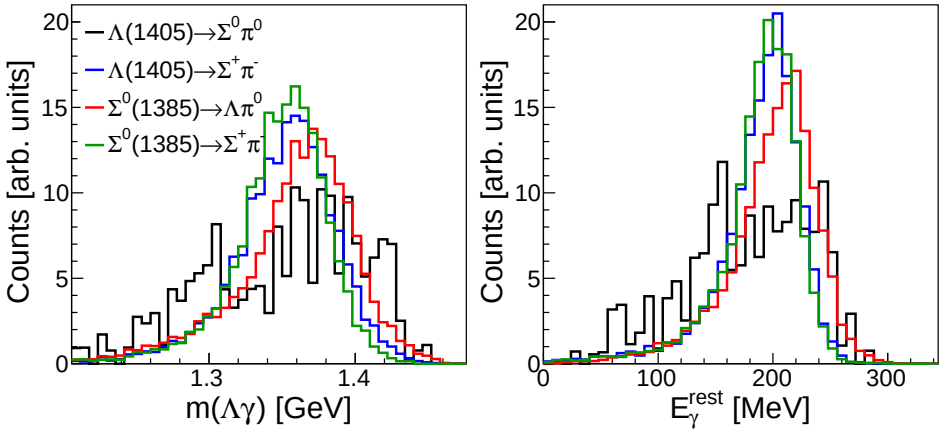

Figure 23: Left side: $m(\Lambda\gamma)$ distributions (arb. scaling) in the $\Lambda(1405)\rightarrow \Lambda\gamma$ analysis for the background caused by the $\Lambda(1405)/\Sigma^0(1385)$ hadronic decays (blue, red and green curves). Right side: Corresponding distributions of the $\Lambda(1405)$ decay photon energy ($\Lambda(1405)$ rest frame).

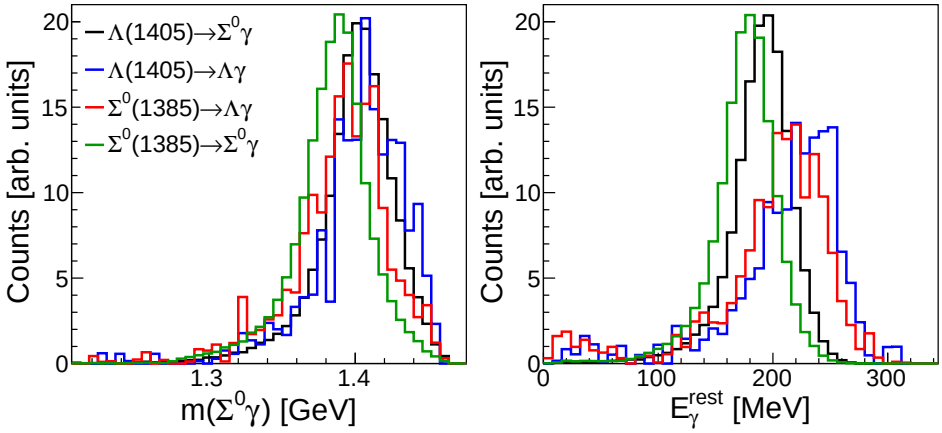

Figure 24: Left side: $m(\Sigma^0\gamma)$ distributions (arb. scaling) in the $\Lambda(1405)\rightarrow \Sigma^0\gamma$ analysis for the signal (black curve) and the background caused by the other $\Lambda(1405)/\Sigma^0(1385)$ radiative decays (blue, red and green curves). Right side: Corresponding distributions of the $\Lambda(1405)$ decay photon energy ($\Lambda(1405)$ rest frame).

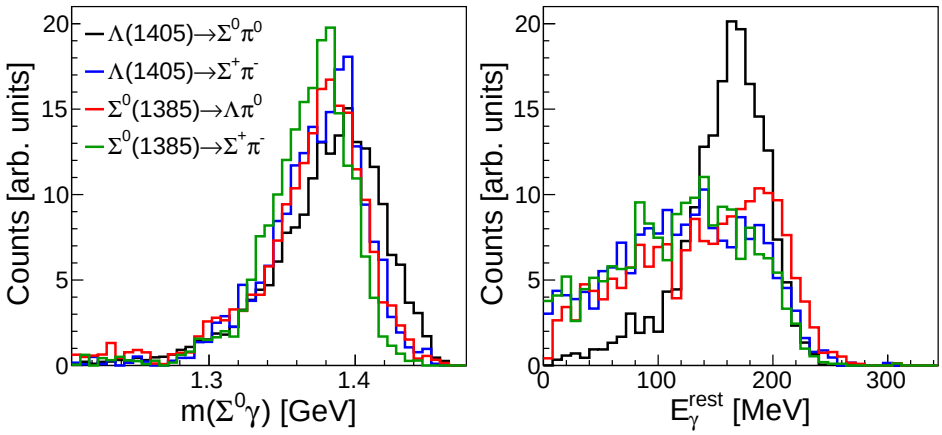

Figure 25: Left side: $m(\Sigma^0\gamma)$ distributions (arb. scaling) in the $\Lambda(1405)\rightarrow \Sigma^0\gamma$ analysis for the background caused by the $\Lambda(1405)/\Sigma^0(1385)$ hadronic decays (blue, red and green curves). Right side: Corresponding distributions of the $\Lambda(1405)$ decay photon energy ($\Lambda(1405)$ rest frame).

References

[1] R. H. Dalitz and S. F. Tuan, Phys. Rev. Lett. **2**, 425 (1959)

[2] M. H. Alston *et al.*, Phys. Rev. Lett. **6**, 698 (1961)

[3] K. A. Olive *et al.* (Particle Data Group), Chin. Phys. C **38**, 090001 (2014)

[4] N. Isgur and G. Karl, Phys. Rev. D **18**, 4187 (1978)

[5] S. Capstick and N. Isgur, Phys. Rev. D **34**, 2809 (1986)

[6] R. N. Faustov and V. O. Galkin, Phys. Rev. D **92**, 054005 (2015)

[7] T. Inoue, Nucl. Phys. A **790**, 530 (2007)

[8] L. S. Kisslinger and E. M. Henley, Eur. Phys. J. A **47**, 8 (2011)

[9] P. J. Fink Jr *et al.*, Phys. Rev. C **41**, 2720 (1990)

[10] J. A. Oller and U.-G. Meißner, Phys. Lett. B **500**, 263 (2001)

[11] D. Jido *et al.*, Nucl. Phys. A **725**, 181 (2003)

[12] T. Hyodo and D. Jido, Prog. Part. Nucl. Phys. **67**, 55 (2012)

[13] Y. Akaishi *et al.*, Nucl. Phys. A **835**, 67 (2010)

[14] R. Molina and M. Döring, arXiv:1512.05831 [hep-lat] (2015)

[15] J. M. M. Hall *et al.*, Phys. Rev. Lett. **114**, 132002 (2015)

[16] D. W. Thomas *et al.*, Nucl. Phys. B **56**, 15 (1973)

[17] R. J. Hemingway, Nucl. Phys. B **253**, 742 (1985)

[18] A. Boyarski *et al.*, Phys. Lett. B **34**, 547 (1971)

[19] J. C. Nacher *et al.*, Phys. Lett. B **455**, 55 (1999)

[20] M. Soyeur and M. F. M. Lutz, Prog. Part. Nucl. Phys. **55**, 165 (2005)

[21] J. K. Ahn, Nucl. Phys. A **721**, 715 (2003)

[22] M. Niiyama *et al.*, Phys. Rev. C **78**, 035202 (2008)

[23] K. Moriya *et al.*, Phys. Rev. C **87**, 035206 (2013)

[24] K. Moriya *et al.*, Phys. Rev. C **88**, 045201 (2013)

[25] K. Moriya *et al.*, Phys. Rev. Lett. **112**, 082004 (2014)

[26] L. Roca and E. Oset, Phys. Rev. C **87**, 055201 (2013)

[27] L. Roca and E. Oset, Phys. Rev. C **88**, 055206 (2013)

[28] M. Mai and U.-G. Meißner, Eur. Phys. J. A **51**, 30 (2015)

[29] C. Fernández-Ramírez *et al.*, Phys. Rev. D **93**, 074015 (2016)

[30] S. Prakhov *et al.*, Phys. Rev. C **70**, 034605 (2004)

[31] I. Zychor *et al.*, Phys. Lett. B **660**, 167 (2008)

[32] G. Agakishiev *et al.*, Phys. Rev. C **87**, 025201 (2013)

[33] W. Roberts and T. Oed, Phys. Rev. C **71**, 055201 (2005)

[34] L. Roca, Nucl. Phys. A **748**, 192 (2005)

[35] D. Krambrich *et al.*, Phys. Rev. Lett. **103**, 052002 (2009)

[36] M. Oberle *et al.*, Phys. Lett. B **721**, 237 (2013)

[37] M. Oberle *et al.*, Eur. Phys. J. A **50**, 54 (2014)

[38] H. Olsen and L. C. Maximon, Phys. Rev. **114**, 887 (1959)

[39] W. Roberts, Phys. Rev. C **73**, 035215 (2006)

[40] S. Taylor *et al.*, Phys. Rev. C **71**, 054609 (2005)

[41] T. Sekihara and S. Kumano, Phys. Rev. C **89**, 025202 (2014)

[42] J. W. Darewych, M. Horbatsch, and R. Koniuk, Phys. Rev. D **28**, 1125 (1983)

[43] H. Burkhardt and J. Lowe, Phys. Rev. C **44**, 607 (1991)

[44] D. A. Whitehouse *et al.*, Phys. Rev. Lett. **63**, 1352 (1989)

[45] L. S. Geng, E. Oset, and M. Döring, Eur. Phys. J. A **32**, 201 (2007)

[46] C. S. An *et al.*, Phys. Rev. C **81**, 045203 (2010)

[47] D. Keller *et al.*, Phys. Rev. D **83**, 072004 (2011)

[48] M. Bazzi *et al.*, Phys. Lett. B **704**, 113 (2011)

[49] K. Piscicchia *et al.*, "Low energy kaon-nuclei interaction studies through the $\Sigma^0\pi^0$ channel with the KLOE detector", Proceedings of International Winter Meeting on Nuclear Physics, January 21–25, 2013, Bormio, Italy. arXiv:1304.7165 [nucl-ex]

[50] S. Kawasaki, "Spectroscopic experiment of $\Lambda(1405)$ via in-flight $d(K^-, n)$ reaction at J-PARC K1.8BR", Talk at the International Conference on Meson-Nucleon Physics and the Structure of the Nucleon (MENU2016), July 25–30, 2016, Kyoto, Japan

[51] H. Sako, "Baryon spectroscopy with $(\pi, 2\pi)$ reactions at J-PARC E45", Talk at the International Workshop on Partial Wave Analysis for Hadron Spectroscopy (PWA 8/ATHOS 3), April 13–17, 2015, Ashburn, VA, USA

[52] T. Nakano, "Recent results from LEPS", Talk at the International Conference on Meson-Nucleon Physics and the Structure of the Nucleon (MENU2016), July 25–30, 2016, Kyoto, Japan

[53] T. C. Jude *et al.*, JPS Conference Proceedings **10**, 032002 (2016)

[54] CLAS12 Technical Design Report, Version 5.1 (2008)

[55] J. Stevens *et al.*, JINST **11**, C07010 (2016)

[56] J. McGeorge *et al.*, Eur. Phys. J. A **37**, 129 (2008)

[57] P. Adlarson *et al.*, Phys. Rev. C **92**, 024617 (2015)

[58] J. Ahrens, private communication (2016)

[59] M. Unverzagt *et al.*, "Decays of the η' Meson", Proposal A2-02/09 for the MAMI Program Advisory Committee, May 2009

[60] A. Starostin *et al.*, Phys. Rev. C **64**, 055205 (2001)

[61] D. Werthmüller *et al.*, Phys. Rev. C **90**, 015205 (2014)

[62] A. Gabler *et al.*, Nucl. Instr. Meth. A **346**, 168 (1994)

[63] D. Watts, Calorimetry in Particle Physics, Proceedings of the 11th International Conference, Perugia, Italy, 2004, World Scientific, Singapore, 560 (2005)

[64] A. Marin *et al.*, Nucl. Instrum. Meth. A **417**, 137 (1998)

[65] T. C. Jude *et al.*, Phys. Lett. B **735**, 112 (2014)

[66] D. Werthmüller, JPS Conference Proceedings **10**, 032008 (2016)

[67] S. Agostinelli *et al.*, Nucl. Instr. Meth. A **506**, 250 (2003)

[68] V. Blobel and E. Lohrmann, Teubner Studienbücher, Teubner (1998)

[69] M. Pivk and F. R. Le Diberder, Nucl. Instr. Meth. A **555**, 356 (2005)

[70] Logbook entry for run 4879, A2 2014 Elog 2014 Entry 19487

[71] Meeting 2014-07-24, A2 DAQ Wiki: meetings:eta_prime_beamplanning:meeting-2014-07-24

[72] W. J. Briscoe, W. Gradl, and I. I. Strakovsky, "Photoproduction of the light scalars $a_0(980)$ and $f_0(980)$ on light nuclei", Letter of Intent A2-04/13 for the MAMI Program Advisory Committee, October 2013